

Multi-Physics Bayesian Analysis of Neutron Star Crust Using Relativistic Mean-Field Model

Vishal Parmar^{1*} and Ignazio Bombaci^{1,2}

¹ INFN, Sezione di Pisa, Largo B. Pontecorvo 3, I-56127 Pisa, Italy and

² Dipartimento di Fisica, Università di Pisa, Largo B. Pontecorvo, 3 I-56127 Pisa, Italy

(Dated: January 13, 2026)

We study the properties of neutron-star crust within a Bayesian framework based on a unified relativistic mean-field (RMF) description of dense matter. The analysis focuses on the posterior distributions of crust properties, constrained by nuclear experimental data, chiral effective field theory, and multimessenger neutron-star observations. In the inference, the outer crust is fixed using the AME2020 nuclear mass table, supplemented by Hartree–Fock–Bogoliubov mass models, while the inner crust is described using a compressible liquid-drop model consistently coupled to the RMF interaction. The same RMF framework is used to describe the uniform core, ensuring a unified treatment across all density regimes. From the resulting posteriors, we extract key crustal observables, including the crust–core transition density and pressure, crust thickness, crust mass, and the fractional crustal moment of inertia. We find that the transition density is primarily governed by the symmetry-energy slope L and curvature K_{sym} evaluated at sub-saturation densities, while the transition pressure plays a central role in determining global crustal properties. The inner-crust equation of state reflects a collective interplay between isovector nuclear-matter properties rather than a dependence on any single parameter. We also assess the impact of using matched crust–core constructions and show that they can introduce systematic differences in predicted neutron-star properties when compared with fully unified treatments.

I. INTRODUCTION

Neutron stars (NSs) provide a natural laboratory for exploring the properties of strongly interacting dense matter under conditions far beyond the reach of terrestrial experiments. [1–5]. Formed in the collapse of massive stellar cores [6], or in an electron capture supernova (ECSN) [7, 8], NSs confine matter under extreme conditions, producing a highly stratified interior. The outer layers consist of a solid Coulomb lattice of nuclei embedded in an electron gas; deeper within, the inner crust hosts neutron-rich clusters immersed in a sea of dripped neutrons and electrons, while the core forms a uniform liquid of baryons and leptons. [9–11]. Although the crust contributes only about one percent of the stellar mass, it typically spans ten percent of the radius and therefore strongly influences observable quantities such as pulsar glitches [12], crustal oscillation modes [13], thermal relaxation, and the cooling evolution [14, 15]. A precise understanding of the crust equation of state (EOS) and of the crust–core transition is thus essential for accurately determining NS structure and assessing the impact of the crust on observable stellar properties [16–18].

However, theoretical uncertainties begin already in the outer crust where the absence of measurements for very neutron-rich isotopes introduces unavoidable model dependence [19, 20]. Deeper inside, the inner crust poses an even greater theoretical challenge, as nuclear clusters can assume a variety of geometries under conditions inaccessible to terrestrial experiments, making theoretical modeling essential [21, 22]. In the literature, the inner crust has been predominantly described within the spherical Wigner–Seitz (WS) approximation, where the crystalline lattice is replaced by independent spherical cells [23]. While this approach has proven highly useful and remains the standard framework, it introduces geometric and boundary-condition simplifications that

become increasingly inaccurate as the density approaches the crust–core transition. In particular, the WS construction cannot fully account for lattice effects, non–spherical cluster correlations, or the onset of spatial uniformization, leading to systematic uncertainties in the predicted transition density and pressure [16, 24, 25]. At still higher densities, within the uniform core, the situation remains far from settled: the composition may range from nucleonic matter to the appearance of additional baryonic degrees of freedom or even transitions towards deconfined quark matter, leading to a wide spectrum of possible EOS [2, 25]. As a result, the global structure of a NS, from the surface to the center, is highly sensitive to the assumed microphysics across the entire density range, from subsaturation crustal densities to the supranuclear regime deep in the core. This sensitivity has become increasingly important in light of modern multimessenger constraints, including tidal deformability limits from GW170817 [26, 27], precise mass and radius measurements of massive pulsars such as PSR J0740+6620 [28], PSR J0348+0432 [29] and PSR J1614–2230 [30], PSR J0437–4715 [31], and multiple theoretical/experimental data on nuclear matter (NM) properties [4] which together significantly narrow the range of viable NS matter properties.

While the properties of the uniform core have been extensively studied, the crust remains comparatively less explored because of its greater complexity and the theoretical uncertainties associated with nonuniform matter. General-purpose EOS for supernova and proto–NS simulations often rely on nuclear statistical equilibrium at finite temperature, combined with energy–density functionals and Thomas–Fermi–type approximations in spherical WS cells [25]. For cold, catalyzed NSs, several strategies have been employed to determine the structure of the NS crust within WS approximation [16, 25, 32–35]. Approaches based on the thermodynamical or dynamical spinodal [36] provide useful insight into the onset of instabilities and can estimate the crust–core transition density, but they do not yield the full composition or

* vishal.parmar@pi.infn.it

geometry of the crust. Methods such as Thomas–Fermi (TF) or extended Thomas–Fermi (ETF), that makes full use of the nuclear-physics-informed finite-size terms of the energy functional [34] offer a detailed description but are computationally demanding when applied over wide parameter ranges. Within this landscape, compressible liquid–drop models (CLDMs), developed in [37] have emerged as an efficient and remarkably accurate framework for crust calculations. In a CLDM model, the energy of a WS cell is expressed through bulk, surface, Coulomb, and curvature contributions, with optional shell corrections [19, 32, 33]. When the surface and curvature terms are carefully calibrated to nuclear masses and semi-infinite NM, the model reproduces detailed Thomas–Fermi and density–functional results while remaining computationally inexpensive [34]. More microscopic methods, such as quantum molecular dynamics simulations [38], band structure calculations [39, 40], and quantum Monte Carlo approaches [25], provide valuable insight into the microscopic structure of pasta phases and into transport and superfluid properties. These methods, however, are extremely demanding computationally.

Unlike the uniform core, whose EOS has been extensively explored within Bayesian and statistical frameworks, the NS crust has received far less attention in this regard. This gap is significant because key crustal properties, such as the crust–core transition density and pressure, the crustal thickness, and the fractional moment of inertia, are highly sensitive to the microphysics of nonuniform matter and cannot be reliably quantified without a consistent treatment of uncertainties. In the literature, the crust is constructed by stitching together different models for the outer crust, inner crust, and core, but such matching procedures inevitably introduce inconsistencies since the underlying nuclear interaction is not the same across all regions [41–44]. Recently, efforts have focused on enforcing consistency between the crust and core through meta-modelling techniques, notably via numerical tools such as CUTER, which enable the matching of a nuclear-physics–informed crust to an arbitrary high-density EOS [45]. A physically coherent description requires that the same nuclear energy–density functional be used from the surface to the center. Only recently have a few studies begun to address this issue by examining the statistical dependence of crustal properties on empirical NM parameters. While the majority of such work rely on the CLDM approach [32, 35, 46], most recent work utilize the extended Thomas–Fermi approach based on a wide set of Skyrme functionals, derived from previous nuclear physics inferences and then identifies EOSs which satisfy astrophysical constraints. [34]. All such different calculations show variations in the inner crust EOS and derived crust–core (CC) transition points. Some of the work also attempts to study the CC transition density [36, 47, 48] not necessarily within a statistical framework.

In this context, it becomes essential to construct the NS crust EOS within a fully Bayesian and unified relativistic framework. In this work, we perform a Bayesian analysis of a unified RMF–based EOS that consistently treats the inner crust, and uniform core using the same underlying nuclear interaction. We treat the parameters of the RMF La-

grangian as random variables constrained by empirical saturation properties, nuclear experimental constraints, and multi-messenger NS observations. The outer crust is computed using the AME2020 mass table [49] supplemented with Hartree–Fock–Bogoliubov (HFB) [50] method using the accurately calibrated Brussels–Montreal [51] energy–density functionals, such as BSk26 [52]. The HFB formalism offers a precise and reliable microscopic method for computing nuclear masses, particularly for nuclei far from stability. The inner crust is obtained by combining the RMF bulk interaction with a compressible liquid–drop description of the WS cell. For each sample of the posterior, we refit the surface parameters of the CLDM to the AME2020 atomic mass evaluations. Motivated by the recent Bayesian study of EOS [4] that combines diverse nuclear experimental constraints with astronomical data to avoid over-reliance on any single measurement, we explore how crustal properties, such as the crust–core transition density and pressure, crustal thickness, and crustal moment of inertia, are constrained by current data. We analyze correlations between these quantities and empirical NM parameters, identify combinations most tightly constrained by observations, and provide updated estimates for the transition density and associated best–fit EOS. In addition, we quantitatively assess how individual NM properties influence the crust EOS itself across sub-saturation densities, rather than focusing solely on the transition point. By analyzing correlations and sensitivities, we identify the NM combinations most relevant for shaping the crust EOS and provide updated estimates of the transition density and associated best–fit EOS. Finally, we compare our unified RMF–based Bayesian results with recent Bayesian crust studies [34, 35, 46] in order to assess the robustness of crust–core transition predictions across different theoretical frameworks.

The paper is organized as follows. In Sec. II, we outline the formalism used to construct the outer crust, inner crust, and liquid core of the NS, and briefly summarize the RMF framework and the NS observables of interest. In Sec. III, we describe the nuclear-physics constraints, the construction of the unified EOS, and the Bayesian inference methodology. The results are presented and discussed in Sec. IV. Finally, Sec. V provides a summary and outlook.

II. EQUATION OF STATE

A. Relativistic Mean Field Theory

The relativistic mean-field (RMF) model provides a covariant effective-field-theory description of dense baryonic matter in which nucleons interact through classical mean fields associated with the scalar σ , vector ω_μ , and isovector–vector $\vec{\rho}_\mu$

mesons [53–58]. The RMF Lagrangian is given by

$$\begin{aligned} \mathcal{L} = \bar{\psi} & \left[\gamma^\mu (i\partial_\mu - g_\omega \omega_\mu - \frac{1}{2} g_\rho \vec{\tau} \cdot \vec{\rho}_\mu) - (M - g_\sigma \sigma) \right] \psi \\ & + \frac{1}{2} (\partial_\mu \sigma \partial^\mu \sigma - m_\sigma^2 \sigma^2) - \frac{\kappa}{3!} g_\sigma^3 \sigma^3 - \frac{\lambda}{4!} g_\sigma^4 \sigma^4 \\ & - \frac{1}{4} \omega_{\mu\nu} \omega^{\mu\nu} + \frac{1}{2} m_\omega^2 \omega_\mu \omega^\mu + \frac{\zeta}{4!} g_\omega^4 (\omega_\mu \omega^\mu)^2 \\ & - \frac{1}{4} \vec{\rho}_{\mu\nu} \cdot \vec{\rho}^{\mu\nu} + \frac{1}{2} m_\rho^2 \vec{\rho}_\mu \cdot \vec{\rho}^\mu + \Lambda_v g_\omega^2 g_\rho^2 (\omega_\mu \omega^\mu) (\vec{\rho}_\mu \cdot \vec{\rho}^\mu), \end{aligned} \quad (1)$$

where ψ denotes the nucleon isodoublet, σ is the scalar meson field responsible for medium-induced attraction, ω_μ is the isoscalar–vector field generating short-range repulsion, and $\vec{\rho}_\mu$ is the isovector–vector field governing the response to neutron–proton asymmetry. The corresponding coupling constants (g_σ , g_ω , g_ρ) determine, respectively, the effective nucleon mass, the saturation density and symmetric-matter pressure, and the symmetry energy. The nonlinear σ self-interactions (κ , λ) regulate the incompressibility of NM [59, 60], the ω self-interaction (ζ) softens the high-density EOS and affects the maximum NS mass [61], and the isoscalar–isovector coupling Λ_v controls the density dependence of the symmetry energy through the L and K_{sym} parameters [62]. Further discussion of their separate and joint effects on the NS EOS and structure is available in the literature [63–67]. The detailed procedure to solve the Euler-Lagrange equations and determining pressure and energy is documented in literature and can be found is [57].

B. Outer crust

In the outer crust, the total energy of a charge–neutral WS cell at a given baryon density ρ_b can be written as [9]

$$E_{WS}(A, Z, \rho_b) = E_N(A, Z) + E_L + E_{zp} + E_e, \quad (2)$$

where $E_N(A, Z) = M(A, Z)$ is the nuclear rest–mass contribution. The lattice and zero–point terms are given by [68]

$$E_L = -C_M \frac{(Ze)^2}{R_N}, \quad E_{zp} = \frac{3}{2} \hbar \omega_p u, \quad (3)$$

with $C_M = 0.89593$ the BCC Mandelung constant, $u = 0.51138$ [16], and $R_N = (3/4\pi n_N)^{1/3}$ with $n_N = 1/V_{WS}$. The electron contribution is $E_e = \mathcal{E}_e V_{WS}$, where V_{WS} is the WS-cell volume.

To determine the equilibrium composition, we follow the BPS prescription [69] and identify, at fixed pressure (P), the nucleus (A, Z) that minimizes the Gibbs free energy,

$$G(A, Z, P) = \frac{\mathcal{E}_{WS} + P}{\rho_b}, \quad (4)$$

where $\mathcal{E}_{WS} = E_{WS}/V_{WS}$ and $\rho_b = A/V_{WS}$.

C. Inner crust

With increasing density, nuclei become progressively less bound, and at the neutron–drip point, unbound neutrons begin to populate the continuum. In the inner crust, each WS

cell contains a nuclear cluster embedded in an ultrarelativistic electron gas and a surrounding neutron fluid. The energy of such a configuration can be written as [18, 69]

$$E_{WS} = M_i(A, Z) + E_e + V_{WS}(\varepsilon_g + n_g M_n), \quad (5)$$

where $M_i(A, Z)$ is the mass of the cluster written as

$$M_i(A, Z) = (A - Z)M_n + ZM_p + E_{cl} - V_{cl}(\varepsilon_g + n_g M_n), \quad (6)$$

where M_n , and M_p are the masses of neutron and proton respectively. ε_g , and n_g are the energy density and density of the neutron gas, respectively. V_{cl} and V_{WS} are the volumes corresponding to the cluster and the WS cell. The energy of the cluster at a given isospin asymmetry (α) and density (n_0) reads

$$E_{cl} = E_{bulk}(n_0, \alpha)A + E_{surf} + E_{curv} + E_{coul}, \quad (7)$$

where E_{surf} , E_{curv} , and E_{coul} are surface, curvature and Coulomb energy respectively. While the Coulomb energy within the WS approximation is well known [23], the surface energy becomes the most important parameter within CLDM. Considering the cluster to be spherical, the surface energy is defined as

$$E_{surf} = 4\pi R_0^2 A^{2/3} \sigma(\alpha), \quad (8)$$

where $R_0 = (3/4\pi n_0)^{1/3}$ is related to the cluster density n_0 , and $\sigma(\alpha)$ is the nuclear surface tension that depends on the isospin asymmetry of the cluster. We use the parametrization of surface tension proposed by Ravenhall *et al.* [70] which is obtained by fitting Thomas-Fermi and Hartree-Fock numerical values as,

$$\sigma(\alpha) = \sigma_0 \frac{2^{p+1} + b_s}{Y_p^{-p} + b_s + (1 - Y_p)^{-p}}, \quad (9)$$

where, σ_0, p, b_s are the free parameters and Y_p is the proton fraction inside the cluster. Similar to surface energy, the curvature energy plays an important part in describing the surface and is written as [71]

$$E_{curv} = 8\pi R_0 A^{1/3} \sigma_c. \quad (10)$$

Here σ_c is the curvature tension related to the surface tension σ as [68, 71],

$$\sigma_c = \sigma \frac{\sigma_{0,c}}{\sigma_0} \gamma (\beta - Y_p), \quad (11)$$

with $\gamma = 5.5$ and $\sigma_{0,c}, \beta$ are the parameters which along with the σ_0 and b_s needs to be fitted for a given EOS with the available experimental AME2020 mass table [49] at a fixed value of p . The equilibrium composition of inhomogeneous matter in the inner crust is obtained by minimizing the energy of WS cell per unit volume at a given baryon density ($\rho_b = \rho_n + \rho_p$), where ρ_n and ρ_p represent the neutron and proton density respectively. We use the variational method used in [32, 71]

where the Lagrange multipliers technique is used so that the auxiliary function to be minimized reads as [32, 33]

$$\mathcal{F}(A, I, \rho_0, \rho_g, \rho_p) = \frac{E_{WS}}{V_{WS}} - \mu_b \rho_b, \quad (12)$$

where μ_b is the baryonic chemical potential. A detailed formulaion of the CLDM formalism can be referred from [19, 32, 46, 68]. In this work we use the same formalism as used¹ in [32, 46] modifying it for the case of RMF bulk matter EOS.

D. Liquid core

As the density increases, the solid inner crust eventually gives way to the uniform liquid core. In this region, the energy density of homogeneous matter in β -equilibrium and charge neutrality [72], is

$$\varepsilon_{\text{core}} = \varepsilon_B(\rho_b, \alpha) + \varepsilon_e(\rho_e) + \varepsilon_\mu(\rho_\mu), \quad (13)$$

where ε_B denotes the baryonic contribution. The crust–core transition is identified from the crust side as the density at which the energy density of the inner–crust WS cell becomes equal to that of uniform npe μ matter,

$$\varepsilon_{WS}(\rho_t) = \varepsilon_{npe\mu}(\rho_t). \quad (14)$$

III. BAYESIAN INFERENCE

In the Bayesian approach, the posterior distribution $P(\boldsymbol{\theta} | D, H)$ quantifies the probability of the model parameters $\boldsymbol{\theta}$ after incorporating the data D , and is obtained from

$$P(\boldsymbol{\theta} | D, H) = \frac{L(D | \boldsymbol{\theta}, H) P(\boldsymbol{\theta} | H)}{P(D | H)}. \quad (15)$$

Here, $L(D | \boldsymbol{\theta}, H)$ is the likelihood measuring the agreement between the model and the data, $P(\boldsymbol{\theta} | H)$ is the prior encoding our pre-existing knowledge of the parameters, and $P(D | H)$ is the evidence ensuring proper normalization. We use this framework to combine nuclear and astrophysical constraints and obtain statistically consistent posteriors for the RMF parameter space.

1. Priors

In our Bayesian analysis, the model parameters $\boldsymbol{\theta}$ correspond to the coupling constants of the RMF Lagrangian, including the meson–nucleon couplings, nonlinear self-interaction strengths, and isoscalar–isovector mixing terms.

These parameters determine the saturation properties, symmetry energy, and high-density behavior of the EOS. We adopt uniform priors over broad intervals that encompass the range of physically reasonable RMF parametrizations. The prior ranges used in this work are summarized in Table I.

TABLE I. Uniform prior ranges adopted for the RMF coupling constants in the Bayesian analysis. All quantities are dimensionless, with the exception of k , which has units of MeV.

Parameter	Min	Max
g_σ	8.0	13.0
g_ω	9.0	14.0
g_ρ	9.0	14.0
κ	0.0	0.05
λ	-0.05	0.05
ζ	0.0	0.06
Λ_v	0.0	0.06

2. Constraints

Motivated by the recent analysis of the NS EOS by Tsang *et al.* [4], we adopt a similarly diverse set of constraints that combines nuclear-experimental inputs, empirical saturation properties, NICER radius measurements, and gravitational-wave tidal deformabilities. Using such complementary observables avoids reliance on any single dataset and provides balanced coverage from sub-saturation to supranuclear densities. In our RMF-based Bayesian framework, we further include the low-density chiral EFT band and an additional pulsar mass–radius constraint. The full set of constraints employed in this work is summarized below.

(i)-Nuclear matter properties:- In the symmetric NM (SNM) sector, we take the standard Giant Monopole Resonance (GMR) motivated value $K_0 = 230 \pm 30$ MeV at $\rho_0 \simeq 0.16 \text{ fm}^{-3}$ [75]. At supra-saturation densities, the pressure of SNM is constrained at $\approx 2\rho_0$ by flow analyses of relativistic Au+Au collisions, denoted HIC(DLL) [73] and HIC(FOPI) [74], which provide consistent values for $P_{\text{SNM}}(2\rho_0)$ with uncertainties at the level of a few MeV/fm³. The density dependence of the symmetry energy $J(\rho)$ is constrained using a set of complementary observables that probe well-defined effective densities. At low densities around $\rho \simeq 0.05 \text{ fm}^{-3}$, the electric dipole polarizability (α_D) of ²⁰⁸Pb constrains the symmetry energy [76]. In the region $\rho \simeq 0.10\text{--}0.12 \text{ fm}^{-3}$, independent information from nuclear-mass systematics (Skyrme and DFT analyses) and isobaric analogue states further restricts the symmetry energy [77–79]. Sub-saturation constraints from heavy-ion reactions, including isospin diffusion and neutron/proton spectral ratios, extend coverage up to $\rho \sim 0.4 \rho_0$ [80, 81]. At higher densities approaching and slightly exceeding ρ_0 , charged-pion spectral ratios and neutron/proton elliptic-flow differences provide direct constraints on the symmetry pressure [82, 83]. Taken together, these measurements form a coherent and density-resolved set of constraints on both $J(\rho)$ and $P_{\text{sym}}(n)$ across

¹ <https://github.com/thomascarreau/NSEOS>

TABLE II. Summary of the empirical, theoretical, and observational constraints used in this work.

(i) Nuclear matter properties				
Constraint	Density ρ (fm $^{-3}$)	Observable	Value	Ref.
<i>Symmetric NM (SNM)</i>				
HIC (DLL)	0.32	P_{SNM} (MeV/fm 3)	10.1 ± 3.0	[73]
HIC (FOPI)	0.32	P_{SNM} (MeV/fm 3)	10.3 ± 2.8	[74]
GMR	0.16	K_{sat} (MeV)	230 ± 30	[75]
<i>Symmetry energy and symmetry pressure</i>				
α_D	0.05	$J(\rho)$ (MeV)	15.9 ± 1.0	[76]
<i>Nuclear masses</i>				
Mass (Skyrme)	0.101 ± 0.005	$J(\rho)$ (MeV)	24.7 ± 0.8	[77]
Mass (DFT)	0.115 ± 0.002	$J(\rho)$ (MeV)	25.4 ± 1.1	[78]
IAS	0.106 ± 0.006	$J(\rho)$ (MeV)	25.5 ± 1.1	[79]
<i>Heavy-ion collisions (isospin-sensitive)</i>				
HIC (Iso-diff)	0.035 ± 0.011	$J(\rho)$ (MeV)	10.3 ± 1.0	[80]
HIC (n/p ratio)	0.069 ± 0.008	$J(\rho)$ (MeV)	16.8 ± 1.2	[81]
HIC (π ratio)	0.232 ± 0.032	$J(\rho)$ (MeV)	52 ± 13	[82]
HIC (n/p flow)	0.240	P_{sym} (MeV/fm 3)	12.1 ± 8.4	[83]
(ii) χ EFT constraints at low density				
χ EFT PNM band	$\rho = 0.04\text{--}0.20 \text{ fm}^{-3}$	$E_{\text{SNM}}(n), E_{\text{PNM}}(n)$	10% expansion of Ref. [84]	[84]
(iii) Astrophysical constraints				
Constraint	$M(M_{\odot})$	R (km)	Λ	Ref.
<i>Gravitational-wave observations</i>				
GW170817 (LIGO/Virgo)	1.4		190_{-120}^{+390}	[85]
<i>NICER pulsars</i>				
PSR J0030+0451	$1.34_{-0.16}^{+0.15}$	$12.71_{-1.19}^{+1.14}$		[86]
PSR J0030+0451	$1.44_{-0.14}^{+0.15}$	$13.02_{-1.06}^{+1.24}$		[87]
PSR J0740+6620	$2.07_{-0.07}^{+0.07}$	$12.39_{-0.98}^{+1.30}$		[88]
PSR J0740+6620	$2.08_{-0.07}^{+0.07}$	$13.70_{-1.5}^{+2.6}$		[89]
PSR J0437-4715	$1.418_{-0.037}^{+0.037}$	$11.36_{-0.63}^{+0.95}$		[31]

the range relevant for the NS crust and outer core.

(ii)- χ EFT constraints at low density We use constraints from chiral effective field theory calculations for symmetric NM and pure neutron matter by Drischler *et al.* [84], obtained using many body perturbation theory with several chiral Hamiltonians. To account for theoretical uncertainties and to remain compatible with other *ab initio* calculations, we conservatively expand the χ EFT uncertainty bands by 10 percent. We do not apply pressure constraints, since the density derivative of the energy per nucleon is subject to significant uncertainties at these densities, as discussed in [32].

(iii)- Astrophysical constraints

Gravitational-wave observations: We incorporate constraints from the binary NS merger GW170817, which provides sensitivity to the high-density behavior of the EOS through tidal deformability measurements. For each EOS candidate, stellar masses, radii, and tidal deformabilities are computed self-consistently by solving the Tolman–Oppenheimer–Volkoff equations together with the linear tidal-perturbation equations [90], allowing direct comparison with the GW170817 inferred tidal response. We do not include GW190425 in our analysis, since its large mass asymmetry and weaker tidal information do not provide competi-

tive constraints on the EOS.

Mass–radius measurements: We further constrain the EOS using mass-radius (M-R) information from three well-studied pulsars, PSR J0030+0451 [86, 87], PSR J0740+6620 [88, 89], and PSR J0437–4715 [31]. For PSR J0030+0451 and PSR J0740+6620, NICER pulse-profile modeling provides joint constraints on stellar mass and radius, with PSR J0740+6620 probing the higher-mass regime through its precisely measured radio-timing mass of $M = 2.08 \pm 0.07 M_{\odot}$ [91]. PSR J0437–4715 complements these measurements by sampling the lower-mass region, which is more sensitive to the EOS near saturation density. For all three sources, we construct likelihoods in the M-R plane using kernel density estimation of the published posterior samples and incorporate them directly into our Bayesian analysis.

The complete set of empirical, experimental, and observational inputs employed in our Bayesian analysis is summarized in Table II. We additionally constrain the nuclear saturation density to $\rho_0 = 0.153 \pm 0.005 \text{ fm}^{-3}$ and the energy per nucleon at saturation to $e_0 = -16.1 \pm 0.2 \text{ MeV}$, and require that every EOS in our ensemble supports a maximum NS mass exceeding $2 M_{\odot}$.

TABLE III. Posterior median values and credible intervals for nuclear-matter (NM) parameters at saturation density, namely the incompressibility K_0 , symmetry energy J , slope of the symmetry energy L , and curvature of the symmetry energy K_{sym} , together with neutron-star (NS) observables including the maximum TOV mass M_{max} , the radius and tidal deformability of a canonical $1.4 M_{\odot}$ neutron star ($R_{1.4}$ and $\Lambda_{1.4}$), the dimensionless moment of inertia $I_{1.4}$, and the moment of inertia relevant for PSR J0737–3039A $I_{1.338}$. Each entry reports the posterior median along with the 68% and 95% credible intervals (CI).

Quantity	68% CI	Median	95% CI
Nuclear-matter parameters			
K_0 (MeV)	231.28 – 266.07	251.82	208.54 – 276.19
J (MeV)	31.996 – 35.139	33.361	30.801 – 37.170
L (MeV)	61.118 – 76.106	67.041	56.753 – 89.122
K_{sym} (MeV)	–66.15 – –14.99	–43.44	–79.78 – 17.94
NS observables			
M_{max} (M_{\odot})	2.030 – 2.233	2.102	2.004 – 2.422
$R_{1.4}$ (km)	12.760 – 13.123	12.933	12.610 – 13.347
$\Lambda_{1.4}$	551.57 – 667.75	603.85	511.63 – 744.37
$I_{1.4}/MR^2$	0.3497 – 0.3570	0.3539	0.3448 – 0.3591
$I_{1.338}$ [10^{45} g cm 2]	1.509 – 1.586	1.545	1.479 – 1.632

IV. RESULTS AND DISCUSSIONS

To probe the posterior distribution with high reliability, we rely on the nested-sampling Monte Carlo framework ML-Friends [92, 93], accessed through the UltraNest package [94]. UltraNest employs the slice-sampling [95], which maintains stable convergence even as the dimensionality of the problem increases. The total number of sampling steps is set adaptively: repeated nested-sampling iterations are performed until the Bayesian evidence, $\log Z$, stabilizes to within the required tolerance. This strategy ensures that both posterior estimation and evidence evaluation remain robust throughout the analysis. In total, we generate $\sim 40\,000$ unified EOSs, each of which spans the full density range from the outer crust to several times nuclear saturation density. All constraints listed in Table II are applied directly to these unified EOSs, ensuring that the inference consistently incorporates both the low-density nuclear physics and the high-density astrophysical information.

A. Posterior distribution of EOS and NS properties

We begin by discussing our results for the NM properties and the EOS, focusing on their posterior distributions obtained from the Bayesian analysis. The resulting posterior distributions for the nuclear-matter (NM) parameters at saturation density, as well as key NS observables, are summarized in Table III.

Our inferred NM properties are compatible with several existing studies that combine gravitational-wave and NICER constraints on the NS EOS. In particular, comparison with the recent analysis of Tsang *et al.* [4] shows overall consistency between the posterior ranges, despite differences in the underlying modeling strategy. While that work adopts a meta-model framework and reports slightly higher preferred values of the symmetry energy parameters J and L with $34.9^{+1.7}_{-2.0}$

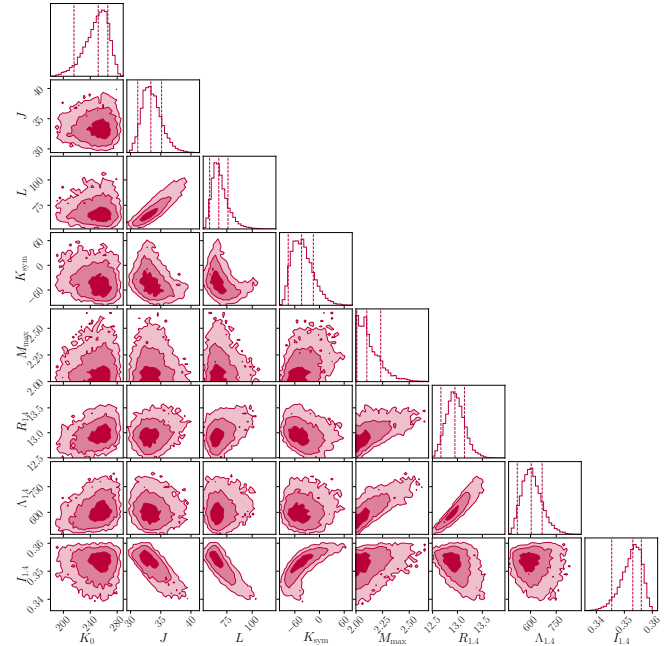


FIG. 1. Marginalized posterior distributions of the nuclear-matter parameters K_0 , J , L , and K_{sym} , and the NS properties M_{max} , $R_{1.4}$, $\Lambda_{1.4}$, and $I_{1.4}$. The diagonal panels show the one-dimensional marginalized posteriors, with vertical lines marking the 68% confidence intervals (CIs). The off-diagonal panels display the two-dimensional joint posteriors, where the filled contour ellipses correspond to the 1σ , 2σ , and 3σ CIs. Darker shades indicate regions of higher probability, while lighter shades represent the broader, lower-probability extensions of the posterior distribution.

and $83.6^{+19.2}_{-16.8}$ MeV, our results remain consistent within uncertainties. We further find that the symmetry incompressibility K_{sym} in our RMF-based analysis tends to favor more negative values, as also found in [96], whereas the meta-model posteriors of Ref. [4] are approximately symmetric between

positive and negative regions. Our inferred incompressibility K_{sat} is slightly higher compared to the values reported by Tsang *et al.* [4], which is typical for RMF-based models once NICER and gravitational-wave constraints, together with the $2M_{\odot}$ maximum-mass requirement, are imposed [96, 97], while remaining well within the allowed range.

For NS properties, we find that the maximum mass spans a relatively wide range, extending up to about $2.5, M_{\odot}$, reflecting residual uncertainties in the high-density EOS. The predicted radius of a $1.4, M_{\odot}$ star is in excellent agreement with the analysis of Tsang *et al.* [4] which finds the radius to be in the range 12.4–13.3 km. In our case, the corresponding credible intervals are 12.60–13.24 km at 95% credibility and 12.76–13.12 km at 68% credibility. The tidal deformability $\Lambda_{1.4}$ is also consistent with both the results of Tsang *et al.* [4] and the constraints inferred from GW170817. In addition, we report the normalized moment of inertia, for which we obtain a 95% credible interval of $0.3448 < I_{1.4} < 0.3591$, with a median value of $I_{1.4} = 0.3539$. Furthermore, PSR J0737–3039A [98] is the primary component of the double-pulsar system, with a precisely measured mass of $M = 1.338 M_{\odot}$. Owing to relativistic spin–orbit coupling in the binary, it is expected that a direct measurement of its moment of inertia will become feasible in the near future, providing a unique and independent probe of the NS EOS [99]. In Table III, we report the inferred moment of inertia of PSR J0737–3039A, characterized by a median value and a corresponding 95% credible interval. When compared with existing theoretical predictions, such as those summarized in Table 1 of [99], our median value is found to be slightly higher than several earlier hadronic and hybrid–EOS estimates obtained from non-unified constructions. Nevertheless, it is in good agreement with the result of Silvia *et al.* [100] and remains well within the overall range spanned by contemporary EOS models. A future precise measurement of the moment of inertia of PSR J0737–3039A would therefore provide a powerful and independent constraint on the NS EOS, with sensitivity not only to the core properties but also to the structure of the crust through its contribution to the stellar radius and mass distribution.

The full joint posterior distribution, including correlations between the EOS parameters and NS properties, is shown in the corner plot in Fig. 1. A strong correlation between the symmetry energy J and its slope parameter L is clearly visible, reflecting their coupled role in determining the isovector sector of the EOS. Among NS observables, the radius $R_{1.4}$ and the tidal deformability $\Lambda_{1.4}$ show a pronounced correlation, as expected from their common dependence on the pressure at intermediate densities. In contrast, the incompressibility K_0 exhibits no strong correlation with the NS properties considered here. Of all stellar observables, the moment of inertia shows the strongest sensitivity to isovector parameters, being substantially affected by the symmetry energy, its slope L , and the curvature parameter K_{sym} . While J and L display an approximately linear negative correlation, K_{sym} tends to show a mild positive correlation with the moment of inertia.

Figure 2 summarizes the EOS and M-R constraints obtained from our Bayesian analysis of unified EOS within RMF

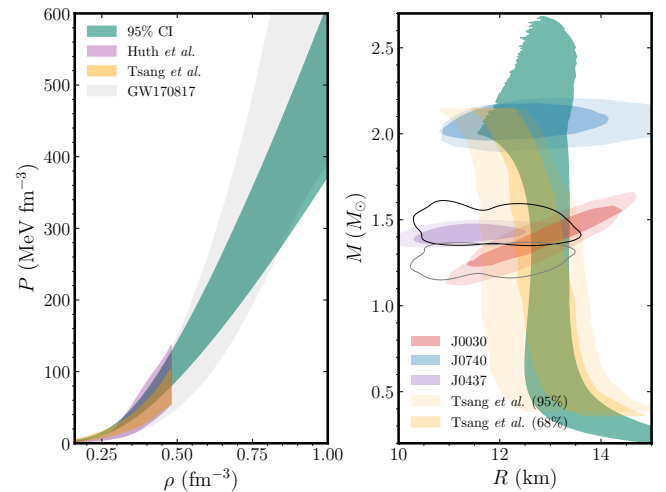


FIG. 2. Left panel: Pressure as a function of baryon density for the ensemble of EOS consistent with all applied constraints. The shaded green band shows the 95% credible interval obtained from our Bayesian analysis. For comparison, we also display the constraints of Huth *et al.* [3] and the multi-physics constrained band reported by Tsang *et al.* [4], together with the pressure constraints inferred from GW170817 [85]. Right panel: Mass–radius relations corresponding to the same EOS ensemble. The green band denotes the 95% credible region obtained from the TOV solutions. Shaded elliptical regions show the mass–radius constraints from NICER pulse-profile modeling for PSR J0030+0451 and PSR J0740+6620, with darker and lighter regions indicating the 68% and 95% credibility intervals, respectively, while PSR J0437–4715 is shown as an additional low-mass constraint. The contours correspond to the GW170817 mass–radius posterior.

framework. The inferred pressure–density band is compatible with gravitational-wave constraints from GW170817 and with representative nuclear-theory results, including those of Huth *et al.* [3] and Tsang *et al.* [4], over the full density range shown. In the M–R plane, our EOS ensemble lies largely within the 95% and 68% credible regions reported by Tsang *et al.*, indicating broad consistency with their analysis. For the most massive NSs, our models predict slightly larger radii than the median Tsang bands, while remaining compatible within uncertainties.

B. Crust Properties

Having established an ensemble of EOSs that is consistent with a broad set of nuclear, gravitational-wave, and X-ray observations, we now turn to the central focus of this work. In the following, we use this vetted EOS ensemble to investigate the properties of the NS crust and its interface with the core. In Fig. 3, we show the main properties of nuclear clusters in the inner crust within the CLDM formalism as functions of the baryon density. Shown are the cluster mass number A , atomic number Z , density of the cluster n_0 , the surrounding neutron gas density n_g , the WS cell radius R_{WS} , and the cluster isospin asymmetry α . The quantum calculations of Negele

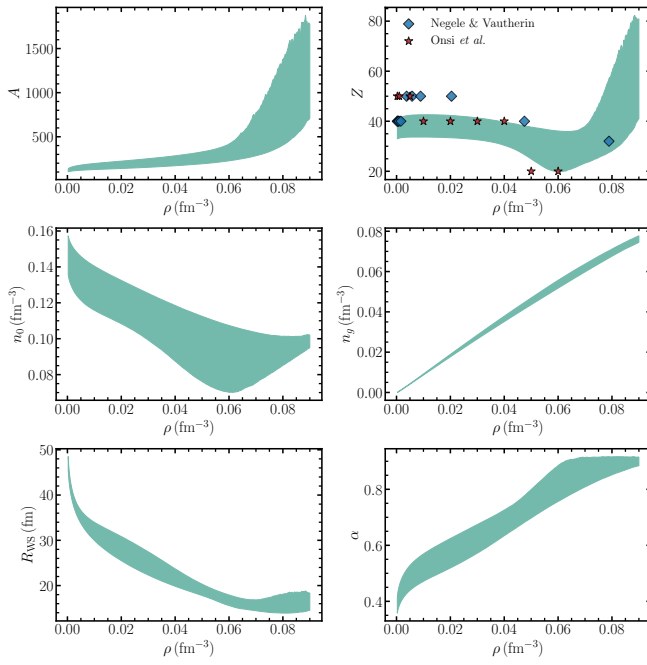


FIG. 3. Properties of nuclear clusters in the inner crust as a function of baryon density ρ inside the crust. Shown are the cluster mass number A (upper left), atomic number Z (upper right), density of the cluster n_0 (middle left), neutron gas density n_g (middle right), the WS cell radius R_{WS} (lower left), and the cluster isospin asymmetry α (lower right). The quantum calculations of Negele and Vautherin [101] and Onsi *et al.* [102] are also shown.

and Vautherin [101] and Onsi *et al.* [102] are shown for comparison for the Z of the cluster. These quantities are sufficient to characterize the structure of the inner crust.

We find that A , Z , and n_0 are strongly model dependent, in line with earlier CLDM studies [32, 46] as well as ETF and [34] microscopic ETFSI calculations [18]. In the low-density region of the inner crust, A increases slowly with density, while it rises more rapidly close to the crust–core transition, indicating the gradual conversion toward homogeneous matter in the core. Owing to the semi-classical nature of the CLDM, Z varies smoothly with density, in contrast to fully quantum approaches such as Negele and Vautherin [101] or Onsi *et al.* [102], and to ETFSI calculations where proton shell corrections produce pronounced step-like features. Nevertheless, the persistent tendency toward $Z \simeq 40$ (which corresponds to a filled proton subshell) throughout the inner crust remains consistent with these quantum results. At the same time, uncertainties arising from NM properties, experimental constraints, and astrophysical data can be larger than typical shell-correction effects, as also discussed in Ref. [32]. Moreover, the evolution of A , Z , and the WS radius R_{WS} directly affects the elastic properties of the inner crust, in particular the shear modulus. Since the shear modulus controls the frequencies of crustal shear modes, these quantities become especially relevant for the interpretation of quasi periodic oscillations observed in magnetar flares.

Among the displayed quantities, the neutron gas density n_g

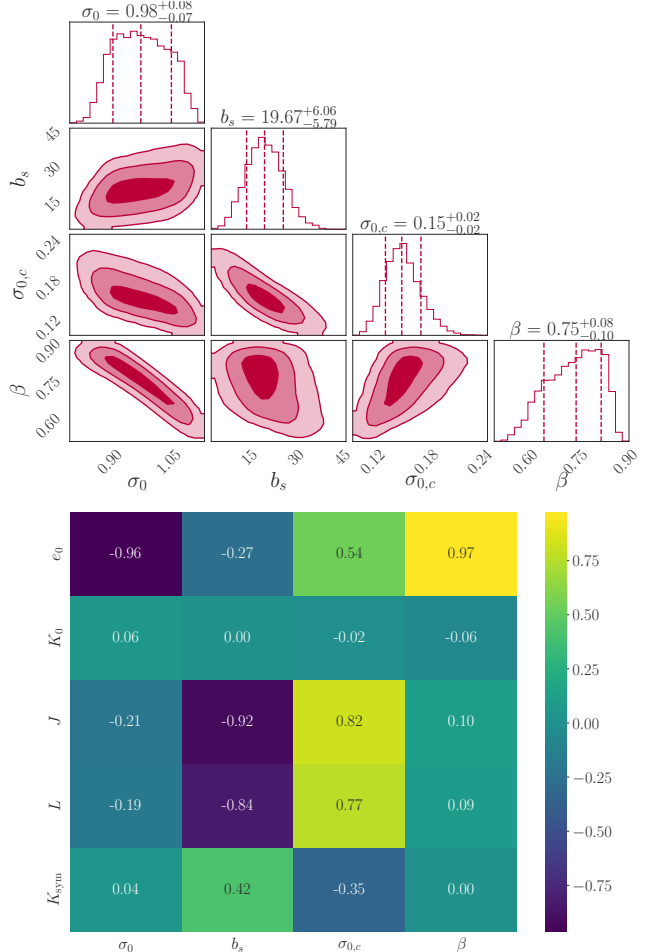


FIG. 4. Posterior distributions of the surface–friction parameters and their correlations with NM properties.

is the least model dependent and increases monotonically with density. We also observe correlated trends, namely a continuous increase of A , a decrease of the cluster central density n_0 , and a reduction of the WS radius R_{WS} with increasing density, together with a steady growth of the asymmetry α . These correlations represent quasi-universal features that have been reported in several crust studies [34, 46, 103, 104] and discussed in [34]. As density increases, clusters become increasingly neutron rich, leading to a systematic rise of α across the inner crust. The behaviour of n_0 , A , and Z can be directly linked to the density dependence of the symmetry energy and its higher-order parameters in the sub-saturation density region, where crust physics is most relevant [19, 105]. Since the inner crust consists of clusters embedded in a neutron gas, its equilibrium configuration follows from energy minimization, making the symmetry energy a key ingredient. An accurate determination of the NM symmetry energy is therefore essential for reliable crust predictions, and conversely, crust properties provide valuable constraints on the symmetry energy. We return to this point in more detail in the following sections.

The structure of the NS inner crust is strongly controlled

by the parametrization of the surface and curvature energies of nuclear clusters (see Eqs. (8) and (10)). Since the surface properties of extremely neutron-rich nuclei are not accessible experimentally, we adopt a semiempirical description of the cluster energy, Eq. (7), and calibrate the associated parameters using experimental masses from the AME2020 table [49]. The surface–curvature parameter set $\mathbf{S} = \{\sigma_0, b_s, \sigma_{0,c}, \beta, \gamma, p\}$ is constrained by minimizing the penalty function $\chi^2(\mathbf{S})$ [106], with a systematic theoretical uncertainty of 0.1 MeV [68]. The isospin-dependence parameter is fixed to $p = 3$, as commonly adopted in surface-energy studies [22, 107], while the curvature parameter is set to $\gamma = 5.5$ following Ref. [71]. The resulting distributions of the optimized surface parameters for the RMF models considered in this work are shown in Fig. 4. The dependence of the surface parameters on the NM properties is shown in the lower panel of Fig. 4.

The surface tension of symmetric NM is tightly constrained to $\sigma_0 = 0.98^{+0.08}_{-0.07}$ MeV fm $^{-2}$, reflecting the strong sensitivity of nuclear binding energies to the overall magnitude of the surface term, which is therefore efficiently fixed by experimental mass data [32, 108]. In contrast, the isovector surface parameter $b_s = 19.7^{+6.1}_{-5.8}$ exhibits a substantially broader posterior distribution, as nuclear masses probe only moderately neutron-rich systems and provide limited constraints on the isospin dependence of the surface energy [32, 71]. The effective surface parameter relevant for clusterized matter near the crust–core transition, $\sigma_{0,c} = 0.15 \pm 0.02$ MeV fm $^{-2}$, is significantly reduced with respect to σ_0 , indicating a pronounced softening of the surface tension in extremely neutron-rich environments, consistent with earlier CLDM and ETF analyses [32, 71]. The asymmetry exponent $\beta = 0.75^{+0.08}_{-0.10}$ is compatible with values commonly adopted in NS crust calculations based on phenomenological surface-energy parametrizations [22, 107]. Furthermore, a strong negative correlation is observed between σ_0 and β , reflecting a compensation mechanism in mass fits whereby an increase in the surface tension of symmetric matter must be accompanied by a steeper isospin dependence in order to reproduce experimental binding energies. A similar correlation is found between the isovector surface parameter b_s and the curvature-related surface term.

In this analysis, the surface parameters exhibit clear correlations with bulk NM properties: the symmetric surface tension σ_0 and the asymmetry exponent β show strong negative and positive correlations, respectively, with the saturation energy e_0 , while the isovector surface parameter b_s and the curvature-related term $\sigma_{0,c}$ display pronounced correlations with the symmetry energy J and its slope L . This behavior contrasts with the meta-modeling study of Ref. [68], where most surface parameters were found to be only weakly correlated with NM properties, with the notable exception of a mild correlation between e_0 and σ_0 . This further signifies that, within the CLDM framework, the use of universal or fixed surface and curvature parameters is generally not justified, as these quantities depend sensitively on the underlying nuclear-matter properties of the adopted interaction. Employing surface parameters calibrated from a different model can therefore lead to a systematic under- or over-estimation of the crust EOS and,

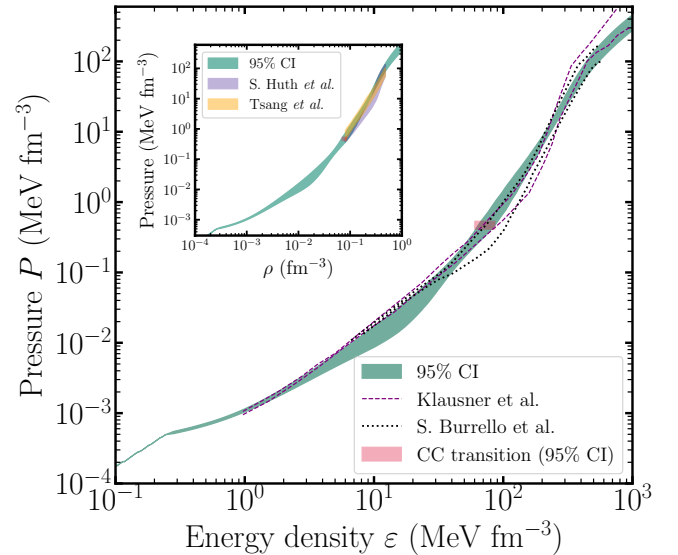


FIG. 5. Pressure as a function of energy density for the unified crust–core EOS obtained from our Bayesian analysis, shown on logarithmic axes to span the full density range from the outer crust to the core. The shaded region denotes the 95% credible interval of the posterior distribution. For comparison, we include the upper and lower bounds from Klausner *et al.* [34] and the microscopic crust calculations of Burrelo *et al.* [35], both converted to consistent units. The inset shows the pressure as a function of baryon density in the crust region, where our results are compared with the constraints of Huth *et al.* [3] and the band of Tsang *et al.* [4]. The magenta band shows the CC transition uncertainty.

in particular, of the crust–core transition density and pressure.

In Fig. 5, we present the fully unified equation of state, with particular emphasis on the neutron-star crust. In our calculations, the outer crust is fixed using the AME2020 atomic mass evaluation together with the HFB24 mass table, thereby minimizing uncertainties associated with nuclear masses. The inner crust predictions are compared with recent crust calculations that incorporate uncertainties from NM properties and astrophysical constraints within a meta–model framework [35], as well as with Skyrme-based results [34]. We note that in the latter case the unified EOS was not included in the inference procedure. The inset shows the pressure as a function of baryon density in the crust, where our posterior EOS is compared with the constraint bands reported by Huth *et al.* [3] and Tsang *et al.* [4]. Our results are in excellent agreement with Tsang *et al.* [4] at low densities and show a mild deviation from the band of Huth *et al.* [3]. This difference can be traced back to the distinct modeling strategies: the analysis of Tsang *et al.* [4] departs from that of Huth *et al.* due to its strict reliance on chiral effective field theory (χ EFT) constraints below $1.5 n_0$, which leads to a systematically softer EOS. In the present work, while we also employ χ EFT constraints at low densities, we relax the corresponding band by 10%, resulting in an EOS that closely follows the behavior reported by Tsang *et al.* [4]. Using this ensemble of EOSs, we further compare our crust predictions with other models in the main panel. We find that the crustal EOS remains strongly model dependent

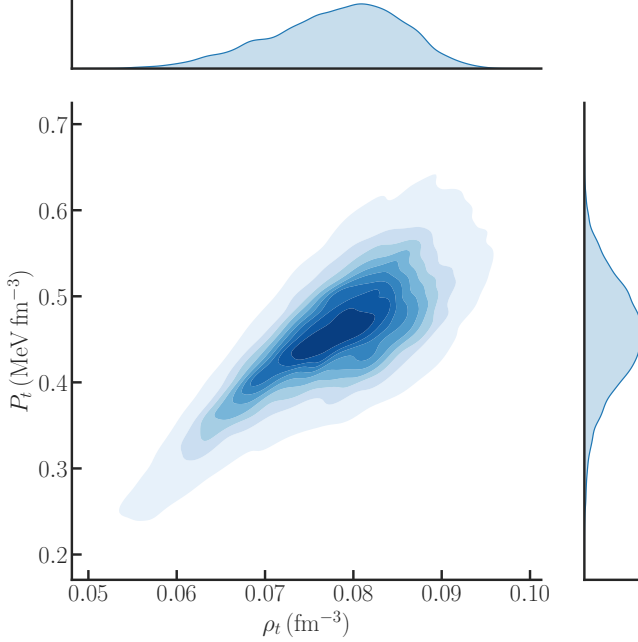


FIG. 6. Kernel density estimate (KDE) of the crust–core transition density ρ_t and transition pressure P_t obtained from the posterior distribution of unified NS EOS. The shaded contours represent the highest-posterior-density (HPD) regions, with darker tones indicating areas of higher probability. The joint distribution highlights the correlated uncertainty between ρ_t and P_t , reflecting the combined influence of nuclear-matter properties and astrophysical constraints on the NS inner crust.

across all three approaches, including the present work. While the different models show good agreement at the lowest densities of the inner crust, significant deviations emerge at intermediate densities. The overall uncertainty is largely driven by the behavior of the density dependence of the symmetry energy and its higher-order derivatives, as previously demonstrated in Ref. [19] and many other works on the NS crust. Within the RMF framework adopted here, which offers less flexibility in nuclear-matter properties than meta–model and Skyrme approaches, the resulting EOS is softer at intermediate inner-crust densities and exhibits a broader spread across models. Close to the crust–core transition, however, it becomes marginally stiffer. This behavior implies reduced elastic rigidity and lower shear-mode frequencies in the intermediate crust, while the increased stiffness near the transition favors a higher transition pressure and a thicker, more massive crust, with direct consequences for crustal oscillations and glitch-related observables.

Among all crustal properties, the crust–core transition point is the most critical quantity, as it governs the extent, mass, and elastic response of the neutron-star crust. Figure 6 shows the posterior distributions of the crust–core transition density, ρ_t , and pressure, P_t , while Table IV summarizes the corresponding 95% credible intervals from the present work together with results from other studies of the crust–core transition. In the present RMF analysis, we do not find values of $\rho_t \lesssim 0.05 \text{ fm}^{-3}$ or $\rho_t \gtrsim 0.10 \text{ fm}^{-3}$. Nevertheless, the poste-

TABLE IV. Crust–core transition density n_{cc} and pressure P_{cc} predicted by different microscopic and phenomenological models. Uncertainties denote 68% credible intervals.

Model	$\rho_t [\text{fm}^{-3}]$	$P_t [\text{MeV fm}^{-3}]$
ETF (Skyrme) [34]	$0.090^{+0.010}_{-0.008}$	$0.510^{+0.077}_{-0.082}$
CLDM (Skyrme) [34]	$0.092^{+0.009}_{-0.007}$	$0.520^{+0.055}_{-0.070}$
CLDM (Meta) [35]	$0.074^{+0.014}_{-0.014}$	$0.277^{+0.137}_{-0.137}$
CLDM (RMF, this work)	$0.0788^{+0.0066}_{-0.0086}$	$0.457^{+0.059}_{-0.061}$

rior distribution exhibits a low-density tail extending toward $\rho_t \lesssim 0.065 \text{ fm}^{-3}$. As shown in Table IV, our inferred values of ρ_t are comparable to those obtained using the CLDM and meta–model approaches tuned to reproduce the (χ EFT) [35] but estimate higher values of P_t . Our ρ_t is also slightly lower than the values reported from ETF and CLDM calculations in Ref. [34], while our corresponding P_t remains broadly consistent with their results. Taken together, Fig. 6 and Table IV highlight the significant model dependence and intrinsic complexity involved in modeling the NS crust. In the present work, where the EOS is constrained by a broad and complementary set of nuclear and astrophysical observables, our results indicate that values of ρ_t approaching or exceeding 0.10 fm^{-3} remain incompatible with current constraints.

Since CC transition point is extremely sensitive to the implied EOS, in Fig. 7, we investigate the correlations between NM properties and the crust–core transition density ρ_t and pressure P_t . Such correlations have been extensively studied in the literature using a variety of approximations, modeling strategies, and statistical frameworks for the EOS [18, 19, 32, 68, 105, 109, 110]. These studies have argued that, rather than the symmetry energy J itself, the slope L and curvature K_{sym} of the symmetry energy play a more important role in determining the crust–core transition [19, 109], motivating the present analysis. Since NS crusts reside at sub-saturation densities, it is also more appropriate to examine correlations between ρ_t and P_t and NM properties evaluated below saturation density, as emphasized in Ref. [110]. This is further justified by the fact that most terrestrial symmetry-energy observables probe sub-saturation densities around $\rho \simeq (2/3)\rho_0$. Accordingly, Fig. 7 is organized such that the left (right) block shows correlations with NM properties evaluated at saturation density ρ_0 ($\rho_0/2$), while the left (right) panels correspond to ρ_t (P_t).

From the full Bayesian inference constrained by a broad set of nuclear and astrophysical observations, we find no significant correlation between the symmetry energy J and either ρ_t or P_t at saturation density. The correlation of J with P_t shows a strong enhancement when evaluated at $\rho_0/2$, while its impact on ρ_t remains weak. In contrast, the slope parameter L exhibits a clear correlation with ρ_t , which remains quantitatively similar when evaluated at $\rho_0/2$ while changing the relationship from non-linear to linear. The influence of L on P_t is generally weak in both cases. For the curvature parameter K_{sym} , the correlation with ρ_t is non-linear and relatively weak at saturation density, but becomes significantly stronger when evaluated at $\rho_0/2$, highlighting the importance of sub-

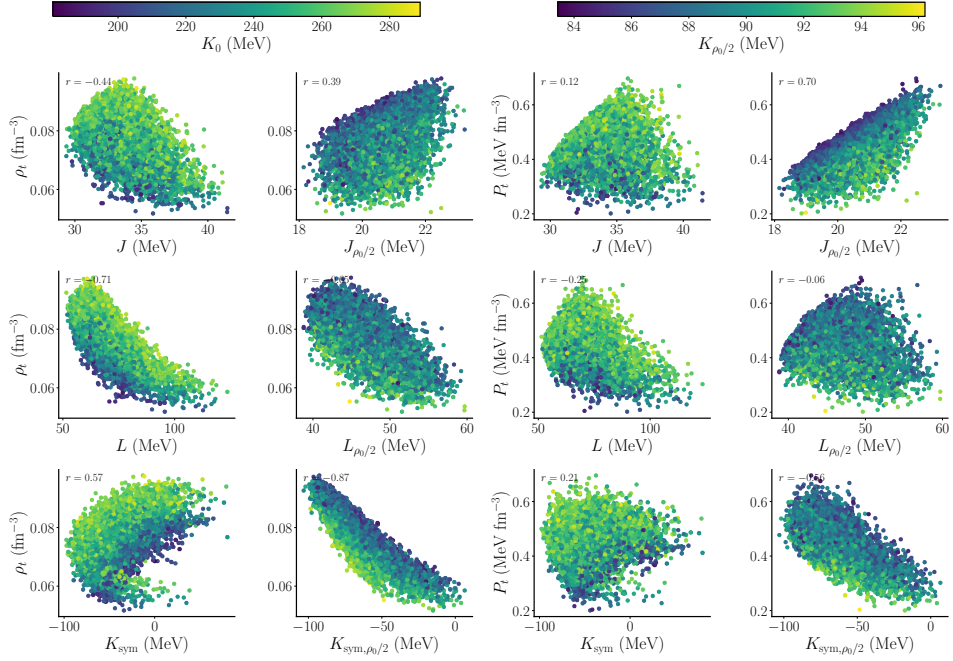


FIG. 7. Correlations of the crust–core transition density ρ_t (left block) and transition pressure P_t (right block) with NM properties evaluated at saturation density and at $\rho_0/2$. From top to bottom, the rows show correlations with the symmetry energy J , its slope L , and the curvature parameter K_{sym} . In each row, the left (right) panel corresponds to the quantity evaluated at saturation density ($\rho_0/2$). The color scale indicates the incompressibility K_0 (left block) and $K_{\rho_0/2}$ (right block). Pearson correlation coefficients are reported in each panel.

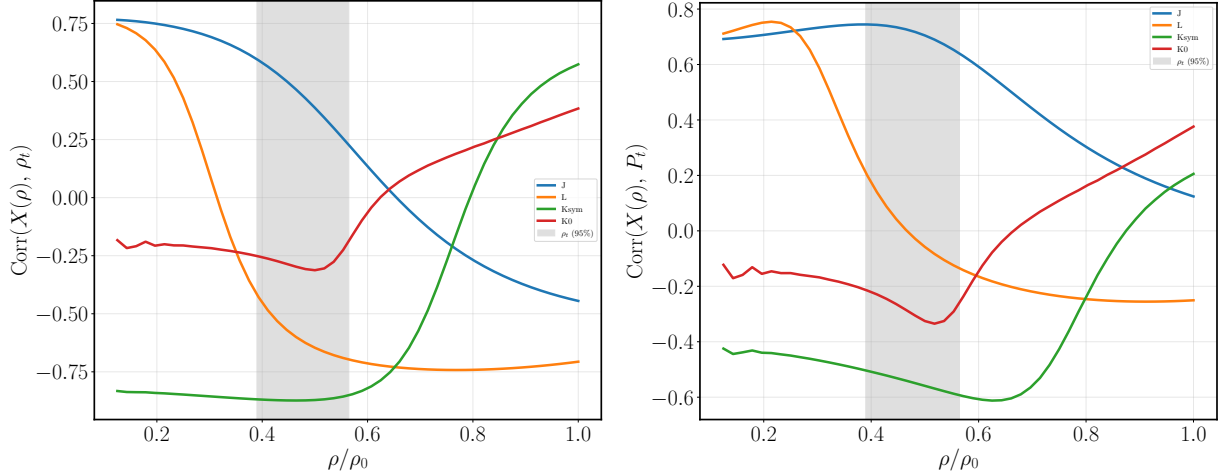


FIG. 8. Correlations of the crust–core transition density ρ_t (left block) and transition pressure P_t (right block) with NM properties evaluated at different reference densities. The gray band represent the uncertainty in the CC transition density.

saturation physics for the crust–core transition. Overall, we find that ρ_t shows stronger correlations with NM properties than P_t . The color coding represents the incompressibility K_0 , for which no significant correlation with either ρ_t or P_t is observed, in agreement with previous studies. This behavior highlights the complex and indirect role of incompressibility in determining crust–core transition properties. Furthermore, within the CLDM framework, when the surface and curvature energy parameters are fitted to experimental nuclear masses, we find no significant correlation between these parameters

and the crust–core transition density ρ_t or transition pressure P_t , confirming the findings of Ref. [32].

In Fig. 8, we examine in detail the density dependence of the correlations between the crust–core transition density ρ_t and transition pressure P_t and nuclear-matter properties. To this end, we compute the relevant NM quantities at each density and evaluate their correlations with ρ_t and P_t . It is evident that the correlations of ρ_t and P_t are not strongest at saturation density and exhibit a complex density dependence. The symmetry energy J shows a significant correlation with

ρ_t when evaluated at sub-saturation densities, $\rho/\rho_0 \lesssim 0.4$ (or $\rho \approx 0.06 \text{ fm}^{-3}$), but this correlation rapidly weakens at higher densities. In contrast, compared to correlations evaluated at ρ_0 , the correlations of ρ_t with the slope parameter L and the curvature parameter K_{sym} increase substantially at sub-saturation densities, particularly in the range $\rho/\rho_0 \simeq 0.5\text{--}0.7$. This density interval is especially relevant, as discussed by Tsang *et al.* [4], since NM properties, most notably L , are best constrained around these densities by terrestrial experiments. The incompressibility shows no meaningful correlation with ρ_t or P_t at any density, consistent with previous findings. These results suggest that a combination of the slope L and curvature K_{sym} evaluated at sub-saturation densities around $\rho/\rho_0 \simeq 0.5\text{--}0.7$ provides the most informative connection to the crust–core transition. For reference, the gray band in the figure indicates the posterior range of ρ_t , illustrating that the strongest correlations occur near $\rho/\rho_0 \approx 0.5\text{--}0.7$, where NM properties are simultaneously best constrained. Compared to ρ_t , the transition pressure P_t exhibits a stronger correlation with the symmetry energy J than with the slope parameter L or the curvature parameter K_{sym} . Accordingly, while ρ_t is primarily influenced by L and K_{sym} in the density range $0.5\text{--}0.7 \rho/\rho_0$, the behavior of P_t in the same density region is dominated by J , with a secondary contribution from K_{sym} .

In the literature, several attempts have been made to derive simple algebraic relations for estimating the CC transition density, ρ_t , using bulk NM properties of a given EOS, most commonly evaluated at saturation density. Early work by Ducoin *et al.* [36] proposed a linear anticorrelation between ρ_t and the symmetry energy slope parameter L . Subsequently, Steiner *et al.* [111] suggested a nonlinear parametrization written in terms of rescaled symmetry energy slopes, motivated by the observed curvature in the correlation. These relations established the central role of isovector properties in controlling the transition, although their quantitative accuracy remains limited. Ducoin *et al.* further showed that evaluating NM properties at subsaturation density improves the predictive power, an observation later supported by independent studies such as Ref. [110].

In the present work, we systematically revisit these empirical relations using a large ensemble of RMF EOS that are simultaneously constrained by nuclear experiments and astrophysical observations. Since the correlation between the CC transition density ρ_t and symmetry energy parameters is seen to be strongest at subsaturation densities, in particular around $\rho_0/2$, it is natural to express ρ_t directly in terms of the symmetry energy slope L and curvature K_{sym} evaluated at this density. Instead of assuming a predefined polynomial structure, we searched for an empirical relation that is both physically transparent and statistically reliable. For this purpose, we employed symbolic regression using the PySR² framework, which applies an evolutionary algorithm to identify analytic expressions by balancing algebraic simplicity against predictive accuracy. A key advantage of this method is that no

functional form is imposed a priori, allowing the algorithm to autonomously explore and rank candidate relations.

The input features were (L, K_{sym}) evaluated at $\rho_0/2$, while the training targets were the RMF calculated transition densities ρ_t . The operator set was restricted to elementary algebraic functions to preserve physical interpretability. Across multiple evolutionary populations, several candidate expressions emerged with low complexity and strong statistical performance. Notably, relatively simple expressions were found to perform nearly as well as more elaborate ones, indicating that the dependence of ρ_t on (L, K_{sym}) is compact. The final symbolic regression model adopted in this work, along with a few other analytic functions used in literature, is reported in Table V, together with its diagnostic metrics. The performance comparison presented in Table V shows that the linear relation based solely on L provides the weakest description of the transition density. Allowing for nonlinear dependence in L already improves the agreement, while the explicit inclusion of the symmetry energy curvature K_{sym} leads to a further and significant reduction in the global error measures. At the same time, the maximum percentage error remains comparable across all parametrizations. This indicates that extreme deviations arise from a small subset of EOS at the edges of parameter space and reflects the intrinsic complexity of the CC transition problem.

It has been emphasized extensively in the literature that the EOS of the NS inner crust is strongly influenced by the density dependence of the nuclear symmetry energy. In particular, while the crust–core transition density is seen to correlate more strongly with the symmetry-energy slope and curvature parameters, L and K_{sym} , than with the symmetry energy at saturation J , it remains important to quantify how isovector nuclear matter properties impact the EOS throughout the inner crust. Most previous studies have examined this dependence by correlating the inner crust EOS with NM properties evaluated at saturation density. However, as demonstrated above, the relevant correlations emerge at subsaturation densities characteristic of the crust. Motivated by this, we quantify the impact of isovector NM properties on the inner crust EOS by comparing the energy density and pressure with the symmetry-energy parameters evaluated at the same baryon density. This procedure defines a local parameter space $\{\rho_i, \varepsilon_i, P_i, J_i, L_i, K_{\text{sym},i}\}$, where the nuclear matter properties are consistently calculated at the density ρ_i associated with each EOS point. At each density, we first compute the absolute (Pearson) correlation between the EOS quantities P and ε and the corresponding isovector NM parameters. To isolate the direct sensitivity of the EOS to individual parameters and to account for the strong mutual correlations among J , L , and K_{sym} , we also evaluate the partial correlation coefficients. For example, the partial correlation between the pressure and the symmetry energy J , conditioned on L and K_{sym} , is defined as

$$r^{\text{part}}(P, J) = \text{corr}\left(P - \hat{P}(L, K_{\text{sym}}), J - \hat{J}(L, K_{\text{sym}})\right), \quad (16)$$

where \hat{P} and \hat{J} denote the linear regressions on the remaining variables. Analogous expressions are used for the energy

² <https://github.com/MilesCranmer/PySR>

TABLE V. Parametrizations of the crust–core transition density ρ_t and their diagnostic performance.

toprule Model	Input	Equation	Statistic	Value
(This work)	$L_{\rho_0/2}, K_{\text{sym},\rho_0/2}$	$\rho_t = 0.0654 - 1.16 \times 10^{-4} L_{\rho_0/2} + 8.55 \times 10^{-8} L_{\rho_0/2} K_{\text{sym},\rho_0/2}^2$	RMSE	3.46×10^{-3}
			MAE	2.72×10^{-3}
			Mean	3.57%
			Max	25.14%
Ducoin <i>et al.</i> [36]	L_{ρ_0}	$\rho_t = 0.0963 - 3.75 \times 10^{-4} L_{\rho_0}$	RMSE	9.26×10^{-3}
			MAE	7.91×10^{-3}
			Mean	9.74%
			Max	25.99%
Steiner <i>et al.</i> [111]	L_{ρ_0}	$\rho_t = \frac{L}{30} \left(0.1327 - 0.0898 \frac{L}{70} + 0.0228 \frac{L^2}{70} \right)$	RMSE	6.12×10^{-3}
			MAE	5.05×10^{-3}
			Mean	6.30%
			Max	25.64%

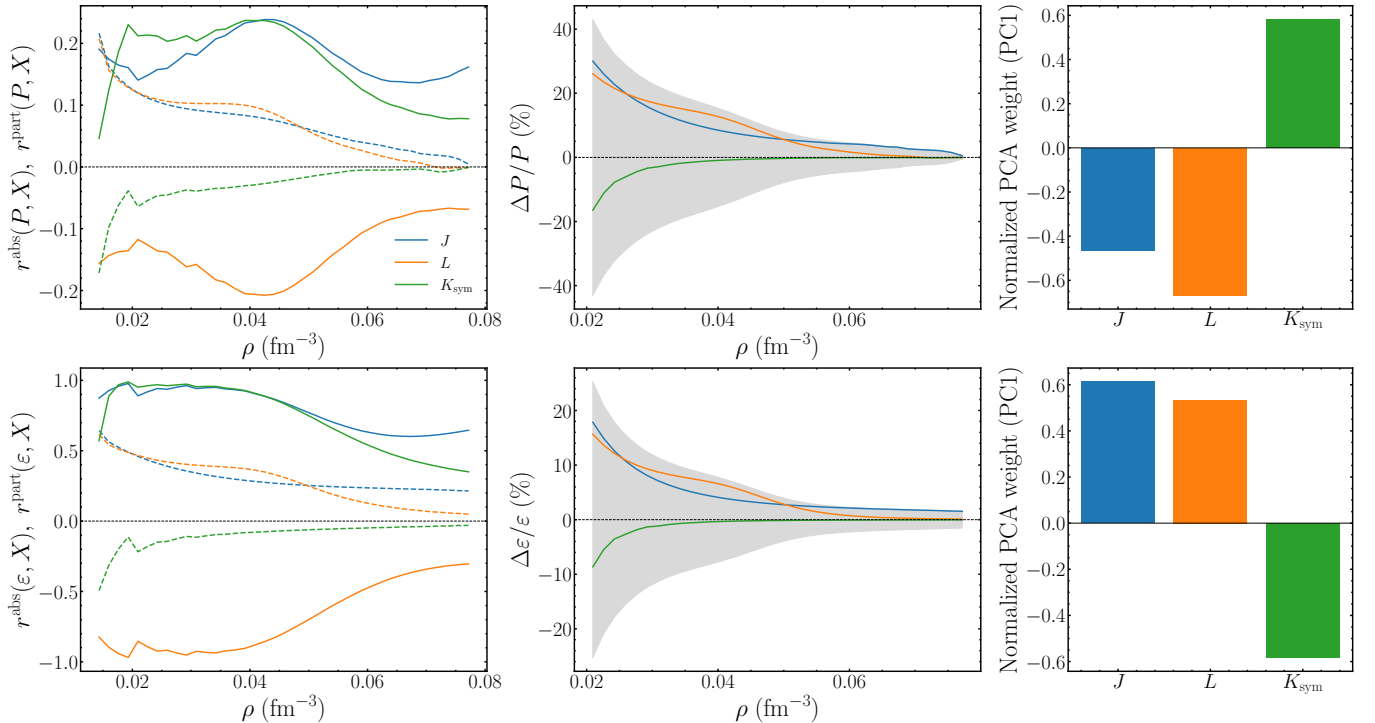


FIG. 9. Sensitivity of the NS inner crust EOS to isovector NM properties as a function of baryon density. The left panels show the absolute (dashed lines) and partial (solid lines) correlations between the pressure P (top) and energy density ε (bottom) and the symmetry-energy parameters J , L , and K_{sym} , all evaluated at the same density. The middle panels display the corresponding induced fractional variations $\Delta P/P$ (top) and $\Delta \varepsilon/\varepsilon$ (bottom). The shaded gray bands indicate the total combined fractional uncertainty, obtained by adding in quadrature the individual contributions from J , L , and K_{sym} . The right panels show the dominant symmetry-energy mode obtained from a principal-component analysis of the local EOS response, highlighting the correlated combinations of J , L , and K_{sym} that primarily govern the pressure and energy density in the inner crust.

density. Finally, the quantitative impact of isovector NM uncertainties on the inner crust EOS is assessed by estimating the induced fractional variations in pressure and energy density, $\Delta P/P$ and $\Delta \varepsilon/\varepsilon$. At each density ρ_i , these variations are obtained by combining the local EOS response to independent variations of the symmetry-energy parameters J , L , and K_{sym} , weighted by their respective dispersions within the posterior.

Specifically, the total fractional variation in the pressure is defined as

$$\left(\frac{\Delta P}{P} \right)_i = \frac{1}{P_i} \left[\left(\frac{\partial P}{\partial J} \sigma_J \right)^2 + \left(\frac{\partial P}{\partial L} \sigma_L \right)^2 + \left(\frac{\partial P}{\partial K_{\text{sym}}} \sigma_{K_{\text{sym}}} \right)^2 \right]^{1/2}, \quad (17)$$

with an analogous expression used to compute $\Delta\varepsilon/\varepsilon$ for the energy density. Here, σ_J , σ_L , and $\sigma_{K_{\text{sym}}}$ denote the standard deviations of the corresponding NM parameters.

In Fig. 9, we summarize the sensitivity of the NS inner crust EOS to isovector NM properties. The left column shows the absolute (dashed lines) and partial (solid lines) correlations between the pressure P (top) and energy density ε (bottom) and the symmetry-energy parameters J , L , and K_{sym} , all evaluated at the same baryon density at which we want to quantify their relations. The middle column displays the corresponding induced fractional variations $\Delta P/P$ and $\Delta\varepsilon/\varepsilon$, with the shaded gray bands indicating the total combined uncertainty obtained by adding in quadrature the individual contributions from the isovector parameters. The right column presents the dominant symmetry-energy modes obtained from a principal-component analysis of the local EOS response. The principal-component analysis (PCA) [112] is performed using the EOS sensitivities evaluated at all densities within the inner crust, such that the resulting modes represent correlated combinations of J , L , and K_{sym} governing the global crust EOS response rather than density-local sensitivities.

While the absolute correlations of the pressure and energy density with the isovector NM parameters are generally weak at different densities, the influence of these parameters becomes significantly more apparent once control variables are introduced through partial correlation analysis. In contrast to the pressure, the energy density of the system is found to be more strongly influenced by the isovector NM properties, particularly at densities below $\rho \simeq 0.06 \text{ fm}^{-3}$. The partial correlation analysis reveals that fixing two of the three isovector parameters exposes a strong conditional dependence of both the pressure and the energy density on the remaining parameter, especially for the energy density. In particular, the slope parameter L shows a consistently stronger influence on both P and ε in the low-density region of the inner crust, although its effect remains comparable in magnitude to those of J and K_{sym} . As can be seen from the correlations, no single NM property dominates the EOS response at any density; instead, the sensitivities arise from competing contributions of all three parameters.

In terms of magnitude, uncertainties in the isovector NM properties can induce variations of up to $\sim \pm 40\%$ in the pressure and $\sim \pm 20\%$ in the energy density at the lower inner crust densities. These variations decrease substantially toward the crust–core transition region, indicating a progressive suppression of isovector uncertainties at higher densities. In the intermediate inner crust region ($\rho \lesssim 0.06 \text{ fm}^{-3}$), the slope parameter L exhibits the largest influence on both P and ε , although not overwhelmingly so compared to the other parameters, while K_{sym} generally shows the smallest quantitative impact. To further quantify this collective behavior, we perform a PCA of the EOS response. The dominant symmetry-energy modes are found to be

$$\delta P \propto -0.466 J - 0.668 L + 0.581 K_{\text{sym}}, \quad (18)$$

$$\delta \varepsilon \propto +0.613 J + 0.534 L - 0.583 K_{\text{sym}}. \quad (19)$$

These dominant modes emphasize that the inner crust EOS is governed by correlated combinations of the symmetry-energy

parameters rather than by any single nuclear matter property. Notably, the effects of the symmetry-energy slope and curvature enter the EOS with opposite signs for the pressure and energy density, leading to partial cancellations in the total response when all isovector parameters vary simultaneously. In particular, variations in L and K_{sym} contribute with opposite trends to P and ε , which further suppresses the net EOS uncertainty despite the strong conditional sensitivities revealed by the partial correlation analysis.

One of the most important observational probes of NS interiors is the occurrence of pulsar glitches, which are sudden spin-up events observed in several rotation-powered pulsars [12, 113]. Among these sources, the Vela pulsar provides the strongest constraint, exhibiting large and quasi-regular glitches that require a substantial angular-momentum reservoir [12]. The standard interpretation attributes these events to the sudden transfer of angular momentum from a neutron superfluid in the inner crust to the solid crust and the rest of the star. For this mechanism to operate, the crust must be sufficiently massive and thick so that it contains a large fraction of the total moment of inertia. Detailed studies have shown that, depending on the crust–core transition density and pressure, the crustal moment of inertia can reach a few percent and, in favorable cases, approach the level required to explain Vela glitches even in the presence of superfluid entrainment [19, 33–35, 46].

In Fig. 10, we show the 95% credible interval bands for the crust thickness l_{crust} , the total crust mass M_{crust} , and the fractional crustal moment of inertia as functions of the NS mass. All these properties are important parameter in various NS calculation such as glitches and cooling [15]. Both the crust thickness and the crust mass decrease monotonically with increasing stellar mass and show an approximately linear trend over the considered mass range. Estimates of the crust thickness and mass obtained from RMF models within the CLDM approach are reported in Table VI. The predicted crust thickness l_{crust} and total crust mass M_{crust} are comparable to the results of [34], obtained using Skyrme energy density functionals within both the ETF and CLDM approaches. Based on the present uncertainties in the NS EOS arising from experimental nuclear observables and astrophysical observations, our results indicate that a NS with a mass of $1.4 M_{\odot}$ is expected to have a crust thickness smaller than about 1.34 km, with a corresponding crust mass below $0.045 M_{\odot}$. This corresponds to 10% of the stellar radius and about 3.2% of the total stellar mass. Furthermore, low-mass neutron stars ($M \lesssim 1.4 M_{\odot}$), whose global properties are already comparatively well constrained, provide a particularly powerful lever for probing the physics of the crust and, in turn, nuclear matter at sub-saturation densities. Owing to steady advances in experimental constraints on nuclear matter and parallel progress in theoretical modeling, the low- and intermediate-density regime of neutron-star matter is now tightly constrained compared to a decade ago. Looking ahead, high-precision mass–radius measurements of low-mass neutron stars, together with NICER-quality observations of canonical $\sim 1.4 M_{\odot}$ pulsars, will offer complementary and highly sensitive information on the crustal mass and thick-

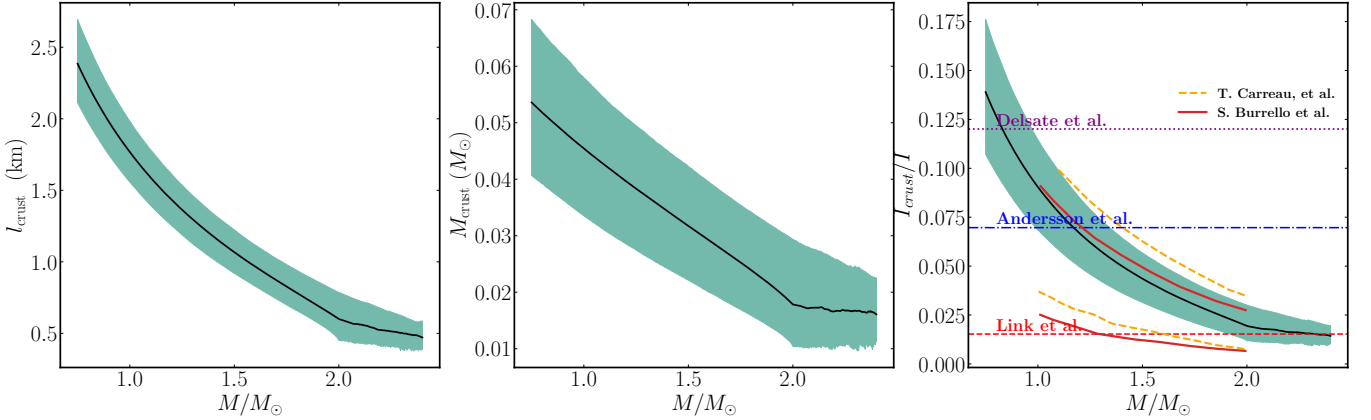


FIG. 10. 95% credible interval bands for the crust thickness L_{crust} , the total crust mass M_{crust} , and the crustal fraction of the moment of inertia I_{crust}/I . Results are shown for the case without superfluid entrainment (solid band) and including entrainment effects using the prescriptions of Link et al., Andersson et al., and Delsate et al. The comparison highlights the impact of entrainment on the effective crustal angular-momentum reservoir.

TABLE VI. Median values and 95% credible intervals for the crust thickness L_{crust} , total crust mass M_{crust} , and fractional crustal moment of inertia I_{crust}/I as functions of the NS mass.

M/M_{\odot}	l_{crust} (km)	M_{crust} (M_{\odot})	I_{crust}/I
1.0	$1.768^{+0.215}_{-0.210}$	$0.04544^{+0.01253}_{-0.0193}$	$0.0904^{+0.0242}_{-0.0219}$
1.2	$1.434^{+0.180}_{-0.180}$	$0.03969^{+0.01125}_{-0.0109}$	$0.0667^{+0.0181}_{-0.0172}$
1.4	$1.177^{+0.159}_{-0.158}$	$0.03435^{+0.01071}_{-0.01015}$	$0.0501^{+0.0145}_{-0.0137}$
1.6	$0.967^{+0.151}_{-0.137}$	$0.02916^{+0.01033}_{-0.00917}$	$0.0378^{+0.0123}_{-0.0108}$
1.8	$0.783^{+0.157}_{-0.125}$	$0.02393^{+0.01029}_{-0.00803}$	$0.0280^{+0.0106}_{-0.0088}$
2.0	$0.601^{+0.185}_{-0.147}$	$0.01784^{+0.01150}_{-0.00738}$	$0.0193^{+0.0107}_{-0.0075}$

ness, enabling significantly sharper tests of crust microphysics and its connection to nuclear matter properties.

In Fig. 10, we also show the posterior distributions of the fractional crustal moment of inertia, I_{crust}/I . We include the limiting case of zero entrainment [114] and scenarios with strong entrainment. The latter is commonly modeled by rescaling the glitch activity parameter of the Vela pulsar by a prefactor of $m_n^*/m_n \simeq 4.6$, following [115], as well as using the more microscopic entrainment estimates of [116]. The basic requirement for explaining glitches within a crust-only superfluid framework is

$$\frac{I_{\text{crust}}}{I} > \mathcal{G}, \quad (20)$$

where \mathcal{G} is the dimensionless glitch activity parameter that quantifies the fraction of the long-term spin-down reversed by glitches. For the Vela pulsar, $\mathcal{G}_{\text{Vela}} \simeq 0.016 \pm 0.002$ [113].

For the strongest entrainment scenario derived from the microscopic calculations of [116], the condition in Eq. (20) is not satisfied for any NS mass, consistent with previous findings [32, 34]. This indicates that, if entrainment is as strong as predicted by these models, a glitch mechanism relying solely on crustal superfluidity is incompatible with observations. For the more widely adopted strong-entrainment prescription with

$m_n^*/m_n = 4.6$ [115], our RMF posterior predicts that the condition $I_{\text{crust}}/I > \mathcal{G}_{\text{Vela}}$ can be satisfied for NS masses below $\sim 1.3 M_{\odot}$. This mass limit is slightly higher than the value of $\sim 1.1 M_{\odot}$ reported in [34]. In contrast, in the absence of entrainment, our RMF models satisfy Eq. (20) over nearly the entire mass range, failing only for very massive stars with $M \gtrsim 2 M_{\odot}$. Furthermore, when compared with the results of [35] and [32], we find that RMF-based crust models tend to support the condition $I_{\text{crust}}/I > \mathcal{G}_{\text{Vela}}$ up to larger NS masses. For completeness, Table VI also reports the 95% credible interval for the fractional crustal moment of inertia, I_{crust}/I . For a canonical $1.4 M_{\odot}$ neutron star, we find a median value of $I_{\text{crust}}/I \simeq 0.05$, indicating that the crust typically stores about 5% of the total stellar moment of inertia within the present uncertainties on NS matter. This value is comparable to the crustal fractional moment of inertia reported in Ref. [34], which was obtained within a Skyrme-based framework under various constraints on dense matter, suggesting a degree of robustness of this result across different nuclear interactions.

Regarding the Vela pulsar, its mass is not yet directly measured and is therefore uncertain. Estimates based on glitch activity and modeling suggest that its mass may lie in the range 1.5 – $1.8 M_{\odot}$, as inferred in Ref. [113]. If such a high mass is assumed, then once strong neutron entrainment is taken into account, the crust alone is insufficient to account for the observed glitch activity. However, in the absence of entrainment, the mass and radius of Vela can still be inferred from the measured glitch activity using our EOS ensemble. The M-R probability distribution can be constructed as [117]

$$p(M, R) = \sum_{\{\vec{P}_{\alpha}\}} p_{\text{post}}(\{\vec{P}_{\alpha}\}) \delta(M_{\alpha} - M) \delta(R_{\alpha} - R), \quad (21)$$

where M_{α} and R_{α} denote the mass and radius obtained for a given EOS parameter set $\{\vec{P}_{\alpha}\}$. For each EOS realization, the stellar configuration is selected by requiring that the central density satisfies the glitch constraint. Here G is sampled from

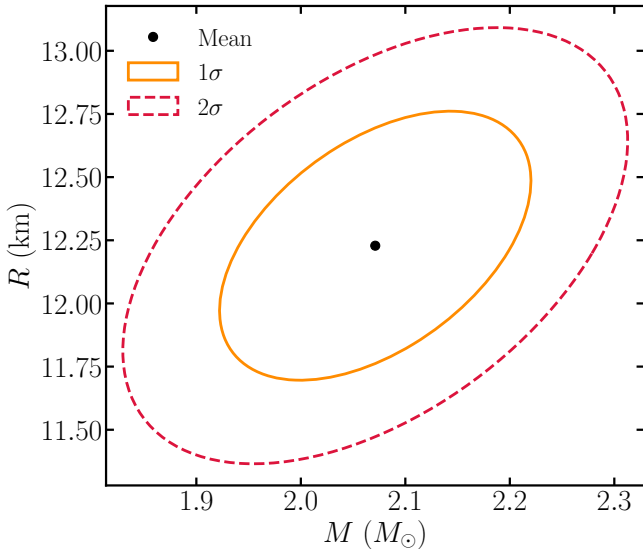


FIG. 11. Mass–radius constraints for the Vela pulsar . The solid and dashed ellipses denote the 1σ and 2σ confidence regions, respectively, constructed from the joint mass–radius probability distribution. The black marker indicates the mean inferred mass and radius.

a Gaussian distribution whose mean and variance are taken from [113]. The resulting 1σ and 2σ confidence ellipses in the mass–radius plane are shown in Fig. 11. Compared to Ref. [113], our allowed region is significantly broader, since that study varied only the entrainment strength while keeping the underlying EOS fixed, whereas we marginalize over the full EOS uncertainty. Notably, the lower-mass edge of our confidence region overlaps with the largest Vela mass reported in Ref. [113], $M = 1.83^{+0.04}_{-0.02} M_{\odot}$, indicating that uncertainties associated with neutron entrainment dominate over EOS uncertainties in setting the Vela glitch constraint. A similar conclusion was also reached in Ref. [117]. Furthermore, in the absence of neutron entrainment, the inferred mass of the Vela pulsar is pushed toward relatively high values, exceeding $1.85 M_{\odot}$ when the present uncertainties in neutron-star matter are taken into account.

Finally, in Fig. 12, we present the joint posterior distributions of the crustal properties, namely, the crust–core transition density ρ_t , transition pressure P_t , crust mass M_{crust} , crust thickness l_{crust} , and fractional crustal moment of inertia I_{crust}/I , together with global NS observables ($R_{1.4}$, $\Lambda_{1.4}$, $I_{1.4}$, and M_{max}) and NM properties in the isovector channel (J , L , and K_{sym}), evaluated at $\rho_0/2$ rather than at saturation density. The figure reveals a rich pattern of correlations, among which several key trends emerge. Most notably, the transition pressure P_t is the dominant crustal quantity, showing strong positive correlations with the crust thickness, crust mass, and the fractional crustal moment of inertia. This behavior reflects the central role of P_t in setting the stiffness of the inner crust and determining its macroscopic contribution to the stellar structure.

For a fixed stellar mass of $1.4 M_{\odot}$, a thicker crust naturally leads to a more massive crust, as evidenced by the tight cor-

relation between l_{crust} and M_{crust} . At the same time, both the crust thickness and mass display only weak or negligible direct correlations with individual NM parameters, reinforcing the conclusion that crust properties are governed by collective effects rather than by any single parameter. The fractional crustal moment of inertia I_{crust}/I shows a clear anticorrelation with the stellar radius $R_{1.4}$ and tidal deformability $\Lambda_{1.4}$, illustrating the sensitivity of crustal observables to the global stellar structure. This behavior suggests that future high-precision radius and tidal measurements may provide indirect but meaningful constraints on crust physics. Finally, evaluating NM properties at $\rho_0/2$ reveals additional insights that are absent when they are defined at saturation density. In particular, the fractional moment of inertia of a $1.4 M_{\odot}$ NS exhibits a noticeable correlation with J when the latter is evaluated at $\rho_0/2$, whereas this correlation is largely suppressed at ρ_0 . Moreover, the total moment of inertia $I_{1.4}$ is found to correlate with both L and K_{sym} at $\rho_0/2$, underscoring the importance of constraining the EOS at sub-saturation densities for an accurate description of NS structure.

C. Unified EOS vs Matched EOS

Finally, we discuss the implications of using unified EOS for deducing the global structure of NSs. Although the crust accounts for only a small fraction of the stellar mass, it plays a non-negligible role in determining global observables such as the radius. As a result, NS modeling often relies on non-unified EOS constructions, in which the core EOS is matched to a separate crust EOS, most commonly based on the BPS model for the outer crust and the Negele–Vautherin EOS for the inner crust [20, 101]. In such approaches, the crust–core transition is implemented by enforcing continuity of pressure and chemical potential at a chosen density, while the underlying nuclear interactions in the two regions remain different. This widely used procedure introduces an intrinsic uncertainty in the predicted stellar radius that depends on both the adopted crust EOS and the matching prescription.

Studies have shown that different matching choices can lead to systematic radius shifts at the level of a few percent, typically $\sim 2\text{--}5\%$, even when the core EOS is fixed [41–43]. With the steadily increasing precision of NS radius measurements from NICER, which already constrain radii at the level of $\sim 0.5\text{--}1$ km for sources such as PSR J0030+0451 and PSR J0740+6620, systematic uncertainties of this magnitude are no longer negligible. This highlights the importance of quantifying and controlling deviations introduced by matched EOS constructions, and motivates the use of unified EOSs for robust interpretation of high-precision NS observations. To quantify the uncertainty associated with unified and matched equations of state, we compare the unified EOS obtained from our posterior with a matched EOS constructed using a standard prescription. For the NS crust, we carefully treat the interface regions. We employ the BPS EOS [20] for the outer crust, corresponding to energy densities in the range $\varepsilon_{\text{min}} \leq \varepsilon \leq \varepsilon_{\text{outer}}$, where $\varepsilon_{\text{min}} = 1.0317 \times 10^4 \text{ g cm}^{-3}$ and $\varepsilon_{\text{outer}} = 4.3 \times 10^{11} \text{ g cm}^{-3}$. In the density region between the

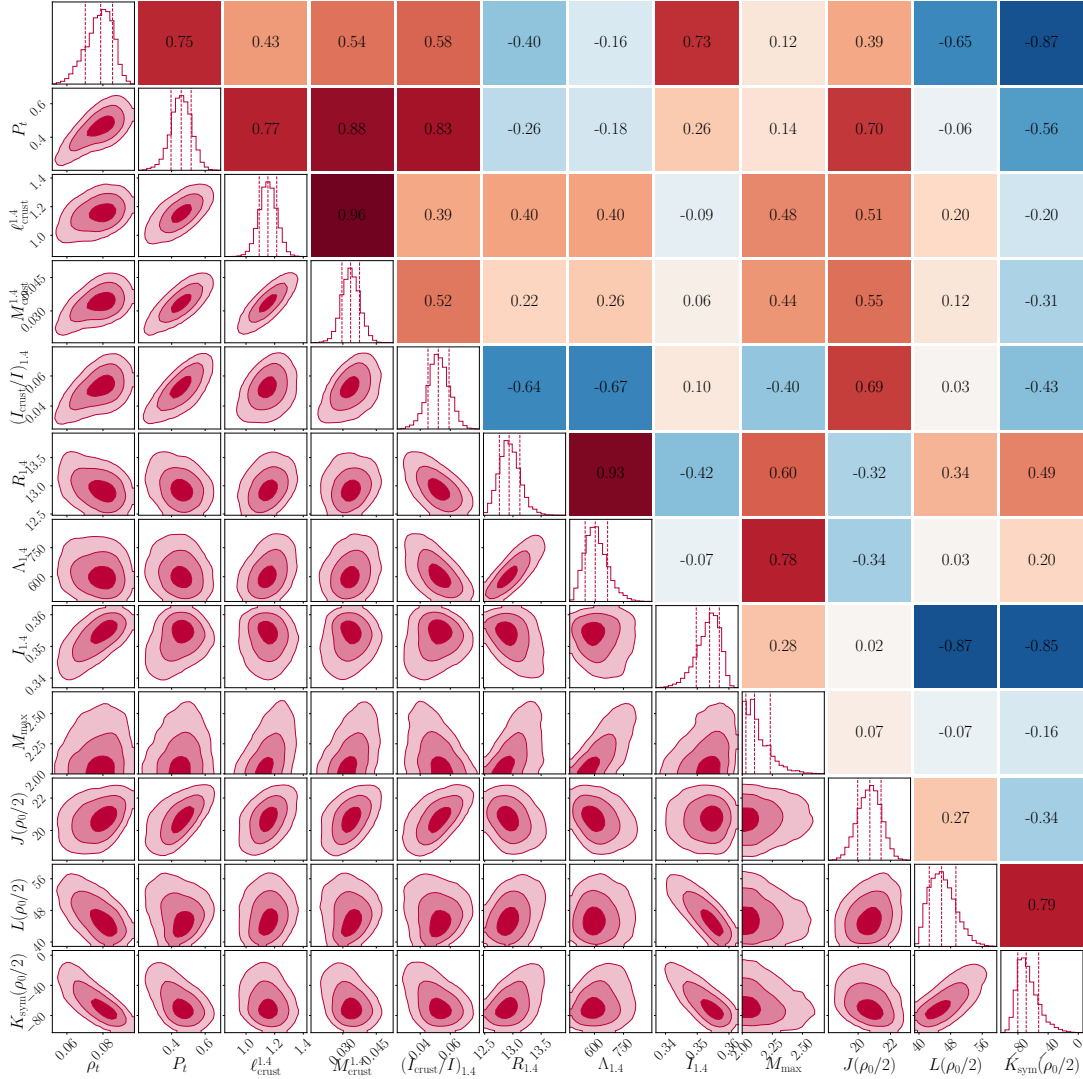


FIG. 12. Corner plot showing the joint posterior distributions of crustal properties (ρ_t , P_t , $l_{\text{crust}}^{1.4}$, $M_{\text{crust}}^{1.4}$, $(I_{\text{crust}}/I)_{1.4}$), global NS observables ($R_{1.4}$, $\Lambda_{1.4}$, $I_{1.4}$, M_{max}), and NM parameters (J , L , K_{sym}). The diagonal panels display the marginalized one-dimensional posterior distributions, while the lower-left panels show the two-dimensional 68% and 95% credible regions. The upper-right panels present the corresponding Pearson correlation coefficients, color-coded to highlight positive (red) and negative (blue) correlations.

outer crust and the core, $\varepsilon_{\text{outer}} < \varepsilon \leq \varepsilon_c$, where ε_c denotes the crust–core transition density, we adopt a polytropic EOS. The complete matched EOS is then defined as [118]

$$P(\varepsilon) = \begin{cases} P_{\text{BPS}}(\varepsilon), & \varepsilon_{\text{min}} \leq \varepsilon \leq \varepsilon_{\text{outer}}, \\ A + B \varepsilon^{4/3}, & \varepsilon_{\text{outer}} < \varepsilon \leq \varepsilon_c, \\ P_{\text{RMF}}(\varepsilon), & \varepsilon > \varepsilon_c, \end{cases} \quad (22)$$

where P_{RMF} denotes the pressure obtained from the RMF framework introduced previously. The parameters A and B are chosen to ensure continuity of the pressure at both $\varepsilon_{\text{outer}}$ and ε_c . The resulting inner crust EOS smoothly interpolates between the outer crust and the core EOS and is finally matched to the core at $\varepsilon_c \simeq 2.14 \times 10^{14} \text{ g cm}^{-3}$.

In Fig. 13, we show the relative difference in the stellar radius between matched and unified EOS for NS masses ranging from $1.2 M_{\odot}$ to $2.0 M_{\odot}$. We find that lower-mass NSs

exhibit the largest spread in radius deviations, indicating that a larger fraction of EOSs display noticeable differences when a matched construction is adopted instead of a unified one. In this mass range, the radius deviation can reach the level of $\sim 2\%$. As the stellar mass increases, the spread in the radius difference progressively narrows, reflecting the diminishing influence of the crust on the global stellar structure. However, for EOSs supporting masses close to $2 M_{\odot}$, the band broadens again. This behavior is a direct consequence of the matching procedure employed here, in which the crust–core transition is imposed at a fixed density rather than being determined self-consistently from the underlying nuclear interaction. Different matching prescriptions, as discussed above, may therefore lead to quantitatively different levels of deviation when compared to a fully unified EOS. Importantly, crust-induced deviations are not confined to low-mass NSs but

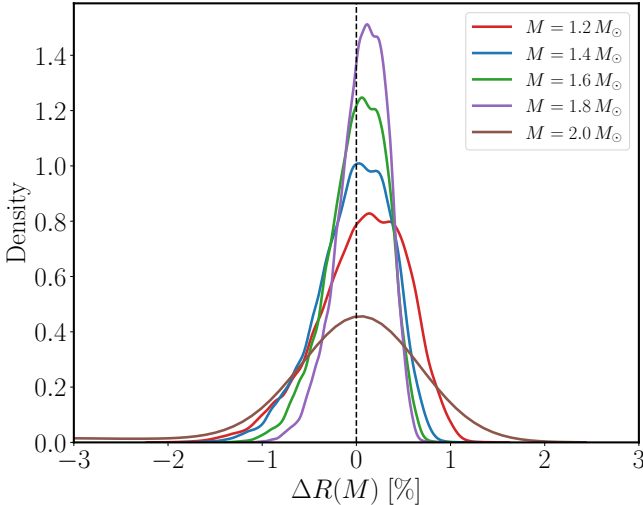


FIG. 13. Kernel density estimates of the relative radius difference $\Delta R(M) = [R_{\text{matched}}(M) - R_{\text{unified}}(M)]/R_{\text{unified}}(M)$ for NSs with fixed masses $M = 1.2, 1.4, 1.6, 1.8$, and $2.0 M_{\odot}$. The vertical dashed line marks $\Delta R(M) = 0$. The distributions are obtained by comparing the radii from the unified EOS construction with those from the original TOV solutions across the full posterior ensemble.

propagate systematically to higher-mass configurations, underscoring the need for an accurate treatment of the crust even in heavy NSs. This becomes particularly relevant in light of the increasing precision of radius measurements from *NICER* and future multi-messenger analyses, where percent-level systematic effects can no longer be neglected. Although the absolute difference in radius remains at the level of a few percent, its impact on the tidal deformability is significantly amplified due to the strong scaling $\Lambda \propto R^5$. Consequently, even modest crust-induced radius variations can lead to appreciable differences in inferred tidal deformabilities, as discussed in Ref. [41]. Since both the crust mass and thickness are highly sensitive to the crust–core transition density, these results further emphasize the importance of a unified treatment of the EOS for robust and consistent NS modeling.

V. SUMMARY AND OUTLOOK

In this work, we perform a Bayesian analysis of neutron-star crust properties using a unified relativistic mean-field (RMF) description of dense matter, incorporating constraints from nuclear experiments, chiral effective field theory, and multimessenger neutron-star observations. Unlike most previous studies, which primarily constrain the uniform core and attach an external crust model, our approach treats the outer crust, inner crust, and liquid core consistently within the same microscopic interaction.

For each sample, the outer crust was constructed using the AME2020 nuclear mass evaluation supplemented by HFB mass tables, while the inner crust was modeled using a compressible liquid-drop model whose surface and curvature parameters were refitted consistently to nuclear masses. The re-

sulting ensemble of unified EOS spans the full density range relevant for neutron stars and satisfies all imposed nuclear and astrophysical constraints.

We obtained predictions for key crust properties, including the crust–core transition density and pressure, crust thickness, crust mass, and the fractional crustal moment of inertia. Our results confirm that the crust–core transition is primarily governed by isovector NM properties, in particular the symmetry energy slope and curvature, rather than by the symmetry energy at saturation or the incompressibility. Evaluating nuclear matter properties at sub-saturation densities, around $\rho_0/2$, significantly strengthens the observed correlations and provides a more physically relevant description of crust physics.

A detailed sensitivity analysis of the inner-crust EOS showed that its behavior is intrinsically collective. Absolute correlations between pressure or energy density and individual NM parameters are generally weak, but partial correlation analysis reveals strong conditional dependencies once correlations among symmetry-energy parameters are accounted for. No single NM parameter dominates the crust EOS at any density; instead, the pressure and energy density arise from competing and partially canceling contributions from the symmetry energy, its slope, and its curvature.

We further quantified the impact of crust physics on global NS observables. The transition pressure was found to be the dominant crustal quantity, strongly correlated with crust thickness, crust mass, and the fractional crustal moment of inertia. For a canonical $1.4 M_{\odot}$ neutron star, our unified models predict that the crust typically contains of order 5% of the total stellar moment of inertia. The corresponding crustal thickness is found to be $\ell_{\text{crust}} = 1.177_{-0.158}^{+0.159}$ km, while the crustal mass amounts to $M_{\text{crust}} = 0.03434_{-0.0101}^{+0.0107} M_{\odot}$. When superfluid entrainment is included, a crust-only explanation of large pulsar glitches remains viable only for relatively low-mass NSs, consistent with earlier studies.

Finally, we explicitly compared unified and matched EOS and demonstrated that commonly used matching prescriptions introduce systematic radius differences at the level of a few percent. While modest in absolute terms, these differences can be amplified in tidal deformabilities and therefore become non-negligible in the context of current high-precision multi-messenger constraints. Our results highlight the importance of unified EOS for reducing systematic uncertainties and for a consistent interpretation of NS observations.

In addition to global crustal properties, microscopic features of the inner crust, such as the shear modulus, its spatial variation, and the possible emergence of nuclear pasta phases, play a central role in shaping the spectrum of crustal oscillations. These ingredients directly affect the frequencies of torsional shear modes and are therefore crucial for interpreting the quasi-periodic oscillations observed in magnetar flares, which provide one of the most direct observational probes of the neutron-star crust and its internal structure. A consistent treatment of the shear response and pasta phases within a unified equation-of-state framework is thus essential for linking theory to observations. We will pursue a detailed investigation of these effects in future work.

[1] E. Annala, T. Gorda, A. Kurkela, and A. Vuorinen, Evidence for quark-matter cores in massive neutron stars, *Nature Physics* **16**, 907 (2020).

[2] E. Annala, T. Gorda, J. Hirvonen, O. Komoltsev, A. Kurkela, J. Nättälä, and A. Vuorinen, Strongly interacting matter exhibits deconfined behavior in massive neutron stars, *Nature Communications* **14**, 8451 (2023).

[3] S. Huth, P. T. H. Pang, I. Tews, T. Dietrich, A. Le Fèvre, A. Schwenk, W. Trautmann, K. Agarwal, M. Bulla, M. W. Coughlin, and C. Van Den Broeck, Constraining neutron-star matter with microscopic and macroscopic collisions, *Nature* **606**, 276 (2022).

[4] C. Y. Tsang, M. B. Tsang, W. G. Lynch, R. Kumar, and C. J. Horowitz, Determination of the equation of state from nuclear experiments and neutron star observations, *Nature Astronomy* **8**, 328 (2024).

[5] A. Marino, C. Dehman, K. Kovlakas, N. Rea, J. A. Pons, and D. Viganò, Constraints on the dense matter equation of state from young and cold isolated neutron stars, *Nature Astronomy* **8**, 1020 (2024).

[6] S. M. Couch, The mechanism (s) of core-collapse supernovae, *Philosophical Transactions of the Royal Society A: Mathematical, Physical and Engineering Sciences* **375**, 20160271 (2017).

[7] Jones, S., Röpke, F. K., Pakmor, R., Seitenzahl, I. R., Ohlmann, S. T., and Edelmann, P. V. F., Do electron-capture supernovae make neutron stars? - first multidimensional hydrodynamic simulations of the oxygen deflagration, *A&A* **593**, A72 (2016).

[8] V. Parmar, D. Scordino, and I. Bombaci, Triggering electron capture supernovae: Dark matter effects in degenerate white-dwarf-like cores of super-asymptotic giant branch stars, *Journal of High Energy Astrophysics* **50**, 100470 (2026).

[9] N. Chamel and P. Haensel, Physics of neutron star crusts, *Living Reviews in Relativity* **11**, 10 (2008).

[10] P. Haensel, J. L. Zdunik, M. Bejger, and J. M. Lattimer, Keplerian frequency of uniformly rotating neutron stars and strange stars, *A&A* **502**, 605 (2009).

[11] Sharma, B. K., Centelles, M., Viñas, X., Baldo, M., and Burgio, G. F., Unified equation of state for neutron stars on a microscopic basis, *A&A* **584**, A103 (2015).

[12] P. M. Pizzochero, M. Antonelli, B. Haskell, and S. Seveso, Constraints on pulsar masses from the maximum observed glitch, *Nature Astronomy* **1**, 0134 (2017).

[13] A. A. Kozhberov and D. G. Yakovlev, Deformed crystals and torsional oscillations of neutron star crust, *Monthly Notices of the Royal Astronomical Society* **498**, 5149 (2020), <https://academic.oup.com/mnras/article-pdf/498/4/5149/33806243/staa2715.pdf>.

[14] A. Potekhin, A. Chugunov, N. Shcheculin, and M. Gusakov, Cooling of neutron stars in soft x-ray transients with realistic crust composition, *Journal of High Energy Astrophysics* **45**, 116 (2025).

[15] D. Page, J. M. Lattimer, M. Prakash, and A. W. Steiner, Minimal cooling of neutron stars: A new paradigm, *APJ Suppl. Series* **155**, 623–650 (2004).

[16] N. Chamel and A. F. Fantina, Binary and ternary ionic compounds in the outer crust of a cold nonaccreting neutron star, *Phys. Rev. C* **94**, 065802 (2016).

[17] X. Roca-Maza and J. Piekarewicz, Impact of the symmetry energy on the outer crust of nonaccreting neutron stars, *Phys. Rev. C* **78**, 025807 (2008).

[18] J. M. Pearson, N. Chamel, A. Y. Potekhin, A. F. Fantina, C. Ducoin, A. K. Dutta, and S. Goriely, Unified equations of state for cold non-accreting neutron stars with Brussels-Montreal functionals – I. Role of symmetry energy, *Monthly Notices of the Royal Astronomical Society* **481**, 2994 (2018).

[19] V. Parmar, H. C. Das, A. Kumar, M. K. Sharma, and S. K. Patra, Crustal properties of a neutron star within an effective relativistic mean-field model, *Phys. Rev. D* **105**, 043017 (2022).

[20] G. Baym, C. Pethick, and P. Sutherland, The Ground State of Matter at High Densities: Equation of State and Stellar Models, *Astrophys. J.* **170**, 299 (1971).

[21] S. S. Avancini, D. P. Menezes, M. D. Alloy, J. R. Marinelli, M. M. W. Moraes, and C. Providência, Warm and cold pasta phase in relativistic mean field theory, *Phys. Rev. C* **78**, 015802 (2008).

[22] S. S. Avancini, L. Brito, J. R. Marinelli, D. P. Menezes, M. M. W. de Moraes, C. Providência, and A. M. Santos, Nuclear “pasta” phase within density dependent hadronic models, *Phys. Rev. C* **79**, 035804 (2009).

[23] N. Chamel and P. Haensel, Physics of neutron star crusts, *Living Reviews in Relativity* **11**, 10 (2008).

[24] N. Chamel, Crustal entrainment and pulsar glitches, *Phys. Rev. Lett.* **110**, 011101 (2013).

[25] M. Oertel, M. Hempel, T. Klähn, and S. Typel, Equations of state for supernovae and compact stars, *Rev. Mod. Phys.* **89**, 015007 (2017).

[26] B. P. Abbott *et al.* (LIGO Scientific Collaboration and Virgo Collaboration), Gw170817: Observation of gravitational waves from a binary neutron star inspiral, *Phys. Rev. Lett.* **119**, 161101 (2017).

[27] B. P. Abbott *et al.* (The LIGO Scientific Collaboration and the Virgo Collaboration), Gw170817: Measurements of neutron star radii and equation of state, *Phys. Rev. Lett.* **121**, 161101 (2018).

[28] H. T. Cromartie, E. Fonseca, S. M. Ransom, P. B. Demorest, Z. Arzoumanian, H. Blumer, P. R. Brook, M. E. DeCesar, T. Dolch, J. A. Ellis, and *et al.*, Relativistic shapiro delay measurements of an extremely massive millisecond pulsar, *Nature Astronomy* **4**, 72–76 (2019).

[29] J. Antoniadis, P. C. C. Freire, N. Wex, T. M. Tauris, R. S. Lynch, M. H. van Kerkwijk, M. Kramer, C. Bassa, V. S. Dhillon, T. Driebe, and *et al.*, A massive pulsar in a compact relativistic binary, *Science* **340**, 1233232 (2013).

[30] P. B. Demorest, T. Pennucci, S. M. Ransom, M. S. E. Roberts, and J. W. T. Hessels, A two-solar-mass neutron star measured using shapiro delay, *Nature* **467**, 1081–1083 (2010).

[31] D. Choudhury, T. Salmi, S. Vinciguerra, T. E. Riley, Y. Kini, A. L. Watts, B. Dorsman, S. Bogdanov, S. Guillot, P. S. Ray, D. J. Reardon, R. A. Remillard, A. V. Bilous, D. Huppenkothen, J. M. Lattimer, N. Rutherford, Z. Arzoumanian, K. C. Gendreau, S. M. Morsink, and W. C. G. Ho, A nicer view of the nearest and brightest millisecond pulsar: Psr j0437–4715, *The Astrophysical Journal Letters* **971**, L20 (2024).

[32] T. Carreau, F. Gulminelli, and J. Margueron, Bayesian analysis of the crust-core transition with a compressible liquid-drop model, *The European Physical Journal A* **55**, 188 (2019).

[33] Carreau, T., Fantina, A. F., and Gulminelli, F., Inner crust of a neutron star at the point of crystallization in a multicomponent

approach, *A&A* **640**, A77 (2020).

[34] P. Klausner, M. Antonelli, and F. Gulminelli, *Neutron star crust informed by nuclear structure data* (2025), arXiv:2505.16929 [nucl-th].

[35] S. Burrello, F. Gulminelli, M. Antonelli, M. Colonna, and A. F. Fantina, Bayesian inference of neutron star crust properties using an ab-initio–benchmark model, *Phys. Rev. C* **112**, 035802 (2025).

[36] C. Ducoin, J. Margueron, C. m. c. Providência, and I. Vidaña, Core–crust transition in neutron stars: Predictivity of density developments, *Phys. Rev. C* **83**, 045810 (2011).

[37] G. Baym, H. A. Bethe, and C. J. Pethick, Neutron star matter, *Nuclear Physics A* **175**, 225 (1971).

[38] C. J. Horowitz and K. Kadau, Breaking strain of neutron star crust and gravitational waves, *Phys. Rev. Lett.* **102**, 191102 (2009).

[39] N. Chamel, Band structure effects for dripped neutrons in neutron star crust, *Nuclear Physics A* **747**, 109 (2005).

[40] K. Sekizawa, S. Kobayashi, and M. Matsuo, Time-dependent extension of the self-consistent band theory for neutron star matter: Anti-entrainment effects in the slab phase, *Phys. Rev. C* **105**, 045807 (2022).

[41] M. Fortin, C. Providência, A. R. Raduta, F. Gulminelli, J. L. Zdunik, P. Haensel, and M. Bejger, Neutron star radii and crusts: Uncertainties and unified equations of state, *Phys. Rev. C* **94**, 035804 (2016).

[42] L. Suleiman, M. Fortin, J. L. Zdunik, and P. Haensel, Influence of the crust on the neutron star macrophysical quantities and universal relations, *Phys. Rev. C* **104**, 015801 (2021).

[43] Davis, P. J., Dinh Thi, H., Fantina, A. F., Gulminelli, F., Oertel, M., and Suleiman, L., Inference of neutron-star properties with unified crust–core equations of state for parameter estimation, *A&A* **687**, A44 (2024).

[44] M. Ferreira and C. Providência, Neutron star properties: Quantifying the effect of the crust–core matching procedure, *Universe* **6**, 10.3390/universe6110220 (2020).

[45] P. J. Davis, H. Dinh Thi, A. F. Fantina, F. Gulminelli, M. Oertel, and L. Suleiman, Crust (unified) tool for equation-of-state reconstruction (cuter) v2, *The European Physical Journal A* **61**, 120 (2025).

[46] Dinh Thi, H., Carreau, T., Fantina, A. F., and Gulminelli, F., Uncertainties in the pasta-phase properties of catalysed neutron stars, *A&A* **654**, A114 (2021).

[47] Douchin, F. and Haensel, P., A unified equation of state of dense matter and neutron star structure, *A&A* **380**, 151 (2001).

[48] X. Viñas, C. Gonzalez-Boquera, B. K. Sharma, and M. Centelles, Unified equation of state for neutron stars within the skyrme–hartree–fock approach, *Acta Physica Polonica B Proceedings Supplement* **10**, 259 (2017).

[49] W. Huang, M. Wang, F. Kondev, G. Audi, and S. Naimi, The AME 2020 atomic mass evaluation (i). evaluation of input data, and adjustment procedures, *Chinese Physics C* **45**, 030002 (2021).

[50] M. Samyn, S. Goriely, P.-H. Heenen, J. M. Pearson, and F. Tondeur, A Hartree–Fock–Bogoliubov mass formula, *Nuclear Physics A* **700**, 142 (2002).

[51] I. O. Eya, J. O. Urama, and A. E. Chukwude, Angular Momentum Transfer and Fractional Moment of Inertia in Pulsar Glitches, *Astrophys. J.* **840**, 56 (2017).

[52] S. Goriely, N. Chamel, and J. M. Pearson, Further explorations of skyrme–hartree–fock–bogoliubov mass formulas. xiii. the 2012 atomic mass evaluation and the symmetry coefficient, *Phys. Rev. C* **88**, 024308 (2013).

[53] B. D. Serot and J. D. Walecka, The Relativistic Nuclear Many Body Problem, *Adv. Nucl. Phys.* **16**, 1 (1986).

[54] W.-C. Chen and J. Piekarewicz, Building relativistic mean field models for finite nuclei and neutron stars, *Phys. Rev. C* **90**, 044305 (2014).

[55] H. Shen, H. Toki, K. Oyamatsu, and K. Sumiyoshi, RELATIVISTIC EQUATION OF STATE FOR CORE-COLLAPSE SUPERNOVA SIMULATIONS, *The Astrophysical Journal* **197**, 20 (2011).

[56] M. Dutra, O. Lourenço, J. S. Sá Martins, A. Delfino, J. R. Stone, and P. D. Stevenson, Skyrme interaction and nuclear matter constraints, *Phys. Rev. C* **85**, 035201 (2012).

[57] M. Dutra, O. Lourenço, S. S. Avancini, B. V. Carlson, A. Delfino, D. P. Menezes, C. Providência, S. Typel, and J. R. Stone, Relativistic mean-field hadronic models under nuclear matter constraints, *Phys. Rev. C* **90**, 055203 (2014).

[58] B. G. Todd-Rutel and J. Piekarewicz, Neutron-rich nuclei and neutron stars: A new accurately calibrated interaction for the study of neutron-rich matter, *Phys. Rev. Lett.* **95**, 122501 (2005).

[59] J. Boguta and A. Bodmer, Relativistic calculation of nuclear matter and the nuclear surface, *Nucl. Phys. A* **292**, 413 (1977).

[60] H. Müller and B. D. Serot, Relativistic mean-field theory and the high-density nuclear equation of state, *Nuclear Physics A* **606**, 508 (1996).

[61] A. Bodmer, Relativistic mean field theory of nuclei with a vector meson self-interaction, *Nuclear Physics A* **526**, 703 (1991).

[62] C. J. Horowitz and J. Piekarewicz, Neutron radii of ^{208}Pb and neutron stars, *Phys. Rev. C* **64**, 062802 (2001).

[63] M. Fortin, S. S. Avancini, C. Providência, and I. Vidaña, Hypernuclei and massive neutron stars, *Phys. Rev. C* **95**, 065803 (2017).

[64] M. Fortin, C. Providência, A. R. Raduta, F. Gulminelli, J. L. Zdunik, P. Haensel, and M. Bejger, Neutron star radii and crusts: Uncertainties and unified equations of state, *Phys. Rev. C* **94**, 035804 (2016).

[65] F. J. Fattoyev and J. Piekarewicz, Sensitivity of the moment of inertia of neutron stars to the equation of state of neutron-rich matter, *Phys. Rev. C* **82**, 025810 (2010).

[66] N. Alam, B. K. Agrawal, M. Fortin, H. Pais, C. Providência, A. R. Raduta, and A. Sulaksono, Strong correlations of neutron star radii with the slopes of nuclear matter incompressibility and symmetry energy at saturation, *Phys. Rev. C* **94**, 052801 (2016).

[67] P. G. Reinhard, The relativistic mean-field description of nuclei and nuclear dynamics, *Reports on Progress in Physics* **52**, 439 (1989).

[68] T. Carreau, *Modeling the (proto)neutron star crust : toward a controlled estimation*, Thèses, Normandie Université (2020).

[69] G. Baym, C. Pethick, and P. Sutherland, The Ground state of matter at high densities: Equation of state and stellar models, *APJ* **170**, 299 (1971).

[70] D. Ravenhall, C. Pethick, and J. Lattimer, Nuclear interface energy at finite temperatures, *Nuclear Physics A* **407**, 571 (1983).

[71] W. G. Newton, M. Gearheart, and B.-A. Li, A survey of the parameter space of the compressible liquid drop model as applied to the neutron star inner crust, *APJ Suppl. Series* **204**, 9 (2013).

[72] N. K. Glendenning, *Compact stars: Nuclear physics, particle physics, and general relativity*, Springer-Verlag New York, 1997.

[73] P. Danielewicz, R. Lacey, and W. G. Lynch, Determination of the equation of state of dense matter, *Science* **298**, 1592 (2002), <https://www.science.org/doi/pdf/10.1126/science.1078070>.

[74] A. Le Fèvre, Y. Leifels, W. Reisdorf, J. Aichelin, and C. Hartnack, Constraining the nuclear matter equation of state around twice saturation density, *Nuclear Physics A* **945**, 112 (2016).

[75] B. G. Todd-Rutel and J. Piekarewicz, Neutron-rich nuclei and neutron stars: A new accurately calibrated interaction for the study of neutron-rich matter, *Phys. Rev. Lett.* **95**, 122501 (2005).

[76] Z. Zhang and L.-W. Chen, Electric dipole polarizability in ^{208}Pb as a probe of the symmetry energy and neutron matter around $\rho_0/3$, *Phys. Rev. C* **92**, 031301 (2015).

[77] B. A. Brown, Constraints on the skyrme equations of state from properties of doubly magic nuclei, *Phys. Rev. Lett.* **111**, 232502 (2013).

[78] M. Kortelainen, J. McDonnell, W. Nazarewicz, P.-G. Reinhard, J. Sarich, N. Schunck, M. V. Stoitsov, and S. M. Wild, Nuclear energy density optimization: Large deformations, *Phys. Rev. C* **85**, 024304 (2012).

[79] P. Danielewicz, P. Singh, and J. Lee, Symmetry energy iii: Isovector skins, *Nuclear Physics A* **958**, 147 (2017).

[80] M. B. Tsang, Y. Zhang, P. Danielewicz, M. Famiano, Z. Li, W. G. Lynch, and A. W. Steiner, Constraints on the density dependence of the symmetry energy, *Phys. Rev. Lett.* **102**, 122701 (2009).

[81] P. Morfouace, C. Tsang, Y. Zhang, W. Lynch, M. Tsang, D. Coupland, M. Youngs, Z. Chajecki, M. Famiano, T. Ghosh, G. Jhang, J. Lee, H. Liu, A. Sanetullaev, R. Showalter, and J. Winkelbauer, Constraining the symmetry energy with heavy-ion collisions and bayesian analyses, *Physics Letters B* **799**, 135045 (2019).

[82] J. Estee, W. G. Lynch, C. Y. Tsang, J. Barney, G. Jhang, M. B. Tsang, R. Wang, M. Kaneko, J. W. Lee, T. Isobe, M. Kurata-Nishimura, T. Murakami, D. S. Ahn, L. Atar, T. Aumann, H. Baba, K. Boretzky, J. Brzychczyk, G. Cerizza, N. Chiga, N. Fukuda, I. Gasparic, B. Hong, A. Horvat, K. Ieki, N. Inabe, Y. J. Kim, T. Kobayashi, Y. Kondo, P. Lasko, H. S. Lee, Y. Leifels, J. Łukasik, J. Manfredi, A. B. McIntosh, P. Morfouace, T. Nakamura, N. Nakatsuka, S. Nishimura, H. Otsu, P. Pawłowski, K. Pelczar, D. Rossi, H. Sakurai, C. Santamaría, H. Sato, H. Scheit, R. Shane, Y. Shimizu, H. Simon, A. Snoch, A. Sochocka, T. Sumikama, H. Suzuki, D. Suzuki, H. Takeda, S. Tangwancharoen, H. Toernqvist, Y. Togano, Z. G. Xiao, S. J. Yennello, Y. Zhang, and M. D. Cozma (S π RIT Collaboration), Probing the symmetry energy with the spectral pion ratio, *Phys. Rev. Lett.* **126**, 162701 (2021).

[83] P. Russotto, P. Wu, M. Zoric, M. Chartier, Y. Leifels, R. Lemmon, Q. Li, J. Łukasik, A. Pagano, P. Pawłowski, and W. Trautmann, Symmetry energy from elliptic flow in 197au+197au, *Physics Letters B* **697**, 471 (2011).

[84] C. Drischler, K. Hebeler, and A. Schwenk, Asymmetric nuclear matter based on chiral two- and three-nucleon interactions, *Phys. Rev. C* **93**, 054314 (2016).

[85] B. P. Abbott and et al. (LIGO & Virgo Collaborations), Gw170817: Observation of gravitational waves from a binary neutron star inspiral, *Physical Review Letters* **119**, 161101 (2017).

[86] T. E. Riley, A. L. Watts, S. Bogdanov, P. S. Ray, R. M. Ludlam, S. Guillot, Z. Arzoumanian, C. L. Baker, A. V. Bilous, D. Chakrabarty, K. C. Gendreau, A. K. Harding, W. C. G. Ho, J. M. Lattimer, S. M. Morsink, and T. E. Strohmayer, A NICER view of PSR J0030+0451: Millisecond pulsar parameter estimation, *APJ* **887**, L21 (2019).

[87] M. C. Miller et al., Psr j0030+0451 mass and radius from nicer data and implications for the properties of neutron star matter, *The Astrophysical Journal Letters* **887**, L24 (2019).

[88] T. E. Riley, A. L. Watts, P. S. Ray, S. Bogdanov, S. Guillot, S. M. Morsink, A. V. Bilous, Z. Arzoumanian, D. Choudhury, J. S. Deneva, K. C. Gendreau, A. K. Harding, W. C. G. Ho, J. M. Lattimer, M. Loewenstein, R. M. Ludlam, C. B. Markwardt, T. Okajima, C. Prescod-Weinstein, R. A. Remillard, M. T. Wolff, E. Fonseca, H. T. Cromartie, M. Kerr, T. T. Pennucci, A. Parthasarathy, S. Ransom, I. Stairs, L. Guillenmot, and I. Cognard, A nicer view of the massive pulsar psr j0740+6620 informed by radio timing and xmm-newton spectroscopy, *The Astrophysical Journal Letters* **918**, L27 (2021).

[89] M. C. Miller and et al., The radius of psr j0740+6620 from nicer and xmm-newton, *The Astrophysical Journal Letters* **918**, L28 (2021).

[90] T. Hinderer, Tidal Love Numbers of Neutron Stars, *Astrophys. J.* **677**, 1216 (2008), arXiv:0711.2420 [astro-ph].

[91] E. Fonseca et al., Refined Mass and Geometric Measurements of the High-mass PSR J0740+6620, *Astro. Phys. J. Lett.* **915**, L12 (2021), arXiv:2104.00880 [astro-ph.HE].

[92] J. Buchner, A statistical test for nested sampling algorithms, *Statistics and Computing* **26**, 383 (2016).

[93] J. Buchner, Collaborative Nested Sampling: Big Data versus Complex Physical Models, *Publications of the Astronomical Society of the Pacific* **131**, 108005 (2019), arXiv:1707.04476 [stat.CO].

[94] J. Buchner, Ultranest - a robust, general purpose bayesian inference engine, *Journal of Open Source Software* **6**, 3001 (2021).

[95] E. Higson, W. Handley, M. Hobson, and A. Lasenby, NESTCHECK: diagnostic tests for nested sampling calculations, *Mon. Not. Roy. Astron. Soc.* **483**, 2044 (2019), arXiv:1804.06406 [stat.CO].

[96] S. M. A. Imam and N. K. Patra, Bayesian analysis of the neutron star equation of state and model comparison: Insights from psr J0437 + 4715, psr J0614 + 3329, and other multiphysics data, *Phys. Rev. D* **112**, 103018 (2025).

[97] Z. Zhu, A. Li, and T. Liu, A bayesian inference of a relativistic mean-field model of neutron star matter from observations of nicer and gw170817/at2017gfo, *The Astrophysical Journal* **943**, 163 (2023).

[98] M. Kramer, I. H. Stairs, R. N. Manchester, M. A. McLaughlin, A. G. Lyne, R. D. Ferdman, M. Burgay, D. R. Lorimer, A. Possenti, N. D'Amico, J. M. Sarkissian, G. B. Hobbs, J. E. Reynolds, P. C. C. Freire, and F. Camilo, Tests of general relativity from timing the double pulsar, *Science* **314**, 97 (2006), <https://www.science.org/doi/10.1126/science.1132305>.

[99] Z. Miao, A. Li, and Z.-G. Dai, On the moment of inertia of psr j0737-3039 a from ligo/virgo and nicer, *Monthly Notices of the Royal Astronomical Society* **515**, 5071 (2022), <https://academic.oup.com/mnras/article-pdf/515/4/5071/45471408/stac2015.pdf>.

[100] H. O. Silva, A. M. Holgado, A. Cárdenas-Avendaño, and N. Yunes, Astrophysical and theoretical physics implications from multimessenger neutron star observations, *Phys. Rev. Lett.* **126**, 181101 (2021).

[101] J. Negele and D. Vautherin, Neutron star matter at sub-nuclear densities, *Nuclear Physics A* **207**, 298 (1973).

[102] M. Onsi, A. K. Dutta, H. Chatri, S. Goriely, N. Chamel, and J. M. Pearson, Semi-classical equation of state and specific-heat expressions with proton shell corrections for the inner crust of a neutron star, *Phys. Rev. C* **77**, 065805 (2008).

[103] Z. Carson, A. W. Steiner, and K. Yagi, Constraining nuclear matter parameters with gw170817, *Phys. Rev. D* **99**, 043010 (2019).

[104] W.-B. Ding, Z. Yu, Y. Xu, C.-J. Liu, and T. Bao, Neutrino

emission and cooling of dark-matter-admixed neutron stars, *Chin. Phys. Lett.* **36**, 049701 (2019).

[105] M. Dutra, C. Lenzi, W. de Paula, and O. Lourenço, Neutron star crustal properties from relativistic mean-field models and bulk parameters effects, *The European Physical Journal A* **57**, 260 (2021).

[106] J. Dobaczewski, W. Nazarewicz, and P.-G. Reinhard, Error estimates of theoretical models: a guide, *Journal of Physics G: Nuclear and Particle Physics* **41**, 074001 (2014).

[107] J. M. Lattimer and F. Douglas Swesty, A generalized equation of state for hot, dense matter, *Nuclear Physics A* **535**, 331 (1991).

[108] K. Pomorski and J. Dudek, Nuclear liquid-drop model and surface-curvature effects, *Phys. Rev. C* **67**, 044316 (2003).

[109] B.-A. Li and M. Magno, Curvature-slope correlation of nuclear symmetry energy and its imprints on the crust-core transition, radius, and tidal deformability of canonical neutron stars, *Phys. Rev. C* **102**, 045807 (2020).

[110] L. E. Balliet, W. G. Newton, S. Cantu, and S. Budimir, Prior probability distributions of neutron star crust models, *The Astrophysical Journal* **918**, 79 (2021).

[111] A. W. Steiner, S. Gandolfi, F. J. Fattoyev, and W. G. Newton, Using neutron star observations to determine crust thicknesses, moments of inertia, and tidal deformabilities, *Phys. Rev. C* **91**, 015804 (2015).

[112] M. Greenacre, P. J. F. Groenen, T. Hastie, A. I. D'Enza, A. Markos, and E. Tuzhilina, Principal component analysis, *Nature Reviews Methods Primers* **2**, 100 (2022).

[113] W. C. G. Ho, C. M. Espinoza, D. Antonopoulou, and N. Andersson, Pinning down the superfluid and measuring masses using pulsar glitches, *Science Advances* **1**, e1500578 (2015), <https://www.science.org/doi/10.1126/sciadv.1500578>.

[114] B. Link, R. I. Epstein, and J. M. Lattimer, Pulsar constraints on neutron star structure and equation of state, *Phys. Rev. Lett.* **83**, 3362 (1999).

[115] N. Andersson, K. Glampedakis, W. C. G. Ho, and C. M. Espinoza, Pulsar glitches: The crust is not enough, *Phys. Rev. Lett.* **109**, 241103 (2012).

[116] T. Delsate, N. Chamel, N. Gürlebeck, A. F. Fantina, J. M. Pearson, and C. Ducoin, Giant pulsar glitches and the inertia of neutron star crusts, *Phys. Rev. D* **94**, 023008 (2016).

[117] T. Carreau, F. Gulminelli, and J. Margueron, General predictions for the neutron star crustal moment of inertia, *Phys. Rev. C* **100**, 055803 (2019).

[118] C. Huang, G. Raaijmakers, A. L. Watts, L. Tolos, and C. Providência, Constraining a relativistic mean field model using neutron star mass-radius measurements I: nucleonic models, *Monthly Notices of the Royal Astronomical Society* **529**, 4650 (2024), <https://academic.oup.com/mnras/article-pdf/529/4/4650/57146443/stae844.pdf>.